AGU PUBLICATIONS

JGR

Journal of Geophysical Research: Earth Surface

RESEARCH ARTICLE
10.1002/2015JF003725

Key Points:
- Coarse grain size distribution and fluid density affects debris flow mobility
- Abundant fines can lead to sustained fluid pressures in excess of hydrostatic
- Sustained excess fluid pressures may arise from reduced particle settling

Correspondence to:
R. Kaitna,
roland.kaitna@boku.ac.at

Citation:
Kaitna, R., M. C. Palucis, B. Yohannes, K. M. Hill, and W. E. Dietrich (2016), Effects of coarse grain size distribution and fine particle content on pore fluid pressure and shear behavior in experimental debris flows, *J. Geophys. Res. Earth Surf.*, *121*, 415–441, doi:10.1002/2015JF003725.

Received 10 SEP 2015
Accepted 13 JAN 2016
Accepted article online 30 JAN 2016
Published online 25 FEB 2016

Effects of coarse grain size distribution and fine particle content on pore fluid pressure and shear behavior in experimental debris flows

Roland Kaitna[1], Marisa C. Palucis[2], Bereket Yohannes[3,4], Kimberly M. Hill[4], and William E. Dietrich[5]

[1]Institute of Mountain Risk Engineering, University of Natural Resources and Life Sciences, Vienna, Austria, [2]Division of Geological and Planetary Sciences, California Institute of Technology, Pasadena, California, USA, [3]School of Engineering, Rutgers, State University of New Jersey, New Brunswick, New Jersey, USA, [4]St. Anthony Falls Laboratory and Department of Civil, Environmental, and Geo-Engineering, University of Minnesota, Twin Cities, Minneapolis, Minnesota, USA, [5]Department of Earth and Planetary Science, University of California, Berkeley, California, USA

Abstract Debris flows are typically a saturated mixture of poorly sorted particles and interstitial fluid, whose density and flow properties depend strongly on the presence of suspended fine sediment. Recent research suggests that grain size distribution (GSD) influences excess pore pressures (i.e., pressure in excess of predicted hydrostatic pressure), which in turn plays a governing role in debris flow behaviors. We report a series of controlled laboratory experiments in a 4 m diameter vertically rotating drum where the coarse particle size distribution and the content of fine particles were varied independently. We measured basal pore fluid pressures, pore fluid pressure profiles (using novel sensor probes), velocity profiles, and longitudinal profiles of the flow height. Excess pore fluid pressure was significant for mixtures with high fines fraction. Such flows exhibited lower values for their bulk flow resistance (as measured by surface slope of the flow), had damped fluctuations of normalized fluid pressure and normal stress, and had velocity profiles where the shear was concentrated at the base of the flow. These effects were most pronounced in flows with a wide coarse GSD distribution. Sustained excess fluid pressure occurred during flow and after cessation of motion. Various mechanisms may cause dilation and contraction of the flows, and we propose that the sustained excess fluid pressures during flow and once the flow has stopped may arise from hindered particle settling and yield strength of the fluid, resulting in transfer of particle weight to the fluid. Thus, debris flow behavior may be strongly influenced by sustained excess fluid pressures controlled by particle settling rates.

1. Introduction

Debris flows are mixtures of sediment and fluid that can transit steep headwater channels and deposit after long runout distances, often at slopes much lower than expected from intrinsic material properties [e.g., *Rickenmann*, 1999]. The grain size distribution of natural debris flows typically includes sediment grain sizes from microns (e.g., clay and silt) to meters (e.g., boulders) and can vary substantially, from mudflows and lahars with a high fraction of fine particles to granular flows with a high fraction of coarse particles. Debris flows are typically distinguished from other modes of mass transport of solid particles by their high volumetric concentration of particles to water, which can exceed 50% [e.g., *Pierson*, 1986]. While the interstitial fluid is water, with the addition of suspended fine particles (typically clay and silt), the flow behavior can differ from that of water [e.g., *Coussot*, 1997] and might better be described as "mud."

Depending on the grain size distribution, several classification schemes have been suggested for these and similar natural particle-fluid flows [e.g., *Johnson*, 1970; *Costa*, 1984; *Takahashi*, 1991; *Coussot and Ancey*, 1999; *Hungr et al.*, 2001]. Here we simply use the phrase "debris flows" to denote natural gravity-driven subaerial particle-fluid flows that span the limiting cases of *mudflows*, which are flows with a high fraction of fine particles, and *granular debris flows*, which have a high fraction of large particles including gravel and boulders. The flow behavior, characterizable in part by flow resistance, is expected to vary dramatically as the grain size distributions vary from mudflows to granular debris flows.

Here we review flow resistance, normal stress, and grain interactions and arrive at a discussion of controls on the generation of excess pore pressures, which appear to strongly influence debris flow behavior. Our review suggests that while theory exists to analyze these controls, experiments on appropriately scaled materials are needed to test and advance further current understanding. Subsequently, we present results of experiments

that led us to propose specific mechanisms for development of excessive pore pressures that may arise from reduced settling in dense fluids.

1.1. Flow Resistance and Dependency on Normal Stress

The flow resistance of granular suspensions and muddy slurries can be described using the Herschel-Bulkley model [e.g., *Herschel and Bulkley*, 1926; *Mueller et al*., 2009; *Coussot*, 1997]. Specifically, the measured shear stress τ scales with strain rate $\dot{\gamma}$ according to

$$\tau = \tau_y + k\dot{\gamma}^a \tag{1}$$

where τ_y is the yield strength (i.e., if $\tau \leq \tau_y$, $\dot{\gamma} = 0$), k is often called the consistency index, and a is power law exponent; typically $a \sim 0.3$ for muddy flows, which are shear thinning [*Coussot*, 1997]. In these flows, there is no apparent dependence of the flow behavior on the local normal stress σ_n or pressure. Many classic debris flow models originating from hydraulics rely on the Herschel-Bulkley model or similar phenomenological relationships that relate shear stress with shear rate independent of normal stress [e.g., *Johnson and Rodine*, 1984; *O'Brien et al*., 1993].

In contrast, the flow resistance in granular flows exhibits a clear dependence on normal stress. This includes a Coulomb-like relation [e.g., *Bagnold*, 1954; *Hungr*, 1995; *Iverson*, 1997]:

$$\tau = \mu\sigma_n \tag{2}$$

where, in *Bagnold's* [1954] classic derivation, the normal and shear stresses scale with shear rate squared, while μ, an effective friction coefficient, is independent of $\dot{\gamma}$. In more recent studies in denser flows [e.g., *Groupement de Recherche Milieux Divisés*, 2004; *Jop et al*., 2006] it is proposed that μ is a function of shear rate, $\dot{\gamma}$, normal stress, σ_n, and properties of the particles themselves (e.g., for a mixture, the average particle density and average particle size [*Yohannes and Hill*, 2010; *Tripathi and Khakhar*, 2011]). For these flows, particle-particle interactions and associated collisional timescales have been associated with the scaling of the effective friction coefficient [*Yohannes and Hill*, 2010].

Various studies have investigated the origin of flow resistance in related grain fluid flows [e.g., *Bagnold*, 1954; *Ancey and Evesque*, 2000; *Armanini et al*., 2005; *Boyer et al*., 2011]. These suggest that shear resistance in grain fluid flows is due to a combination of factors, including frictional resistance due to enduring grain contacts, collisional momentum exchange between the grains, and viscous resistance of the muddy fluid [e.g., *Iverson*, 1997; *Ancey*, 2006]. Based on scaling considerations, *Iverson* [1997] argues that in most natural debris flows shear resistance is most closely associated with interparticle contacts rather than collisional interactions or the viscous interstitial fluid. In all of the cases where collisional and/or frictional particle-particle interactions are important, a significant part of the flow resistance should scale with normal stress [e.g., *Boyer et al*., 2011]. So, to understand the flow behavior, it is necessary to understand the controls on the normal stress.

1.2. Normal Stress and Grain-to-Grain Contacts

To identify the normal stress associated with grain-to-grain contacts in a grain-fluid mixture, Terzaghi's effective stress principle [*Terzaghi*, 1943] is often used. To summarize some salient issues, we consider a simplified case, where the normal stresses are the same in all directions (isotropic). In this case, the local stress associated with grain-to-grain contacts is sometimes expressed as an effective normal stress σ_{eff}, calculated according to

$$\sigma_{\text{eff}} = \sigma_{\text{tot}} - P \tag{3}$$

where σ_{tot} is the total normal stress (associated with the bulk density of the material), and P is pore fluid pressure. In other words, equation (3) expresses a partitioning of the total normal stresses between the solid and fluid phases of the material: σ_{eff} is the part of the total normal stress borne by the particles, and P is the part borne by the fluid. When $P \ll \sigma_{\text{tot}}$, the particle network carries a significant fraction of the stress associated with the total weight of the material, and we expect expressions such as equation (2) to more completely describe the shear resistance of the flow. As $P \rightarrow \sigma_{\text{tot}}$, the effective normal stress approaches zero and we expect the interstitial fluid to bear more of the shear resistance to flow. In that case a phenomenological flow law like that given in equation (1) or a Bagnold-type expression accounting for collisional momentum exchange (as speculated by *Iverson* [2013]) might describe flow resistance. The system can be considered "fully liquefied" when the liquefaction ratio (LR) equals 1, where

$$\text{LR} \equiv P/\sigma_{\text{tot}} \tag{4}$$

The concept of effective stress has been adapted in two-phase debris flow models to separately account for the flow resistance of the solid and fluid components [e.g., *Iverson and Denlinger*, 2001; *Pitman and Le*, 2005;

Pelanti et al., 2008; *Berzi and Jenkins*, 2009; *Iverson and George*, 2014; *Bouchut et al.*, 2015]. This brings to light the relevance of the magnitude of the fluid pressure in a constantly deforming grain-fluid assembly. In steady uniform flows where the free surface is inclined at an angle θ relative to the horizontal and the weight of grains are supported entirely by interparticle contacts, we expect the total stress and the pore fluid pressure to increase with distance from the free surface according to $\sigma_{tot} \sim \rho_b g(H-z)\cos\theta$ and $P_w \sim \rho_w g(H-z)\cos\theta$, where ρ_b and ρ_w are the densities of the bulk material and the water, respectively, g is gravity, H is the total depth of the flow, and z increases from the bed in the normal direction. In other words, in this simple saturated case, we expect that the pore pressure in the pore fluid is equal to the "hydrostatic" fluid pressure (proportional to depth and density of the interstitial fluid, which might be modified due to fine particles in suspension) and that the effective stress scales with the buoyant weight of the particles. However, there is ample evidence in the literature that a nonzero excess pore pressure can develop.

1.3. Development and Dissipation of Excess Pore Pressures

The most commonly cited sources of excess pore pressure in debris flows are associated with natural unsteadiness and nonuniformities. In a particle-fluid flow that progresses down a sloped, rough surface, the particles shear past one another in layers as the bulk mass dilates [*Iverson*, 2005; *Goren et al.*, 2010]. The jostling of the particles in this shear motion creates temporally varying nonuniformities such as local pressure gradients that squeeze the fluid in and out of pore spaces. Because the fluid cannot respond instantaneously, the local fluid pressure may vary significantly in space and time [e.g., *Iverson and LaHusen*, 1989; *Goren et al.*, 2010]. The more viscous the fluid, and/or the smaller the pore spaces, the longer it takes for the fluid to move in response to a local pore pressure gradient (similar to the classic expression for fluid motion in a porous medium [*Darcy*, 1856]). Once a particle-fluid flow dilates, it begins to contract, and subsequently, a locally elevated pore pressure may be maintained over longer timescales. Under the right conditions, *Pierson* [1981] showed that the average pore pressure could be elevated above the hydrostatic case for timescales greater than that of a debris flow event.

Other mechanisms for nonhydrostatic fluid pressure generation proposed in the literature include centripetal acceleration due to a curved channel [e.g., *Chow*, 1959], resistance associated with the yield strength of the muddy pore fluid [e.g., *Hampton*, 1979], and Reynolds stresses [*Hotta and Ohta*, 2000]. Additionally, nonuniformities such as segregation at the front of a debris flow and the development of a boulder-rich front that acts as a "moving dam" for the finer, muddier debris upstream [*Pierson*, 1986] might result in a local peak in stress and excess pore pressure.

The dissipation of excess pore pressure is often considered using a one-dimensional pore pressure diffusion formulation [e.g., *Major*, 2000; *de Haas*, 2015] associated with classic (quasi-static) consolidation theory [*Terzaghi*, 1943]:

$$\frac{\partial P_e}{\partial t} - D\frac{\partial^2 P_e}{\partial z^2} = 0 \tag{5}$$

where P_e is the magnitude of fluid pressure in excess to the simple hydrostatic case, z is the vertical coordinate in the opposite direction of gravity, and D is a diffusion coefficient, defined as $D = kE_c/\eta$, where k is the hydraulic permeability of the porous media, E_c is the modulus reflecting the bulk stiffness of the porous media, and η is the dynamic viscosity of the pore fluid [*Major*, 2000; *Iverson*, 2005]. The development of equation (5) for excess pore pressure is based on a number of assumptions (described in *Major* [2000]) which are appropriate for conditions in wide, thin deposits of saturated, poorly sorted sandy debris subject to low-magnitude stresses. While direct applicability to moving debris flows is not obvious, applying it to quasisteady systems can provide some intuition about how pore pressure dissipation varies from one mixture to the next. Fitting solutions to equation (5) to data from consolidation experiments, *Major* [2000] found diffusion coefficients that varied from $10^{-4}\,m^2/s$ for sandy gravel debris flow deposits down to $10^{-7}\,m^2/s$ for muddy slurries. These results strongly suggest a link between grain size distribution and excess pore pressures: once excess pore pressures are generated in systems containing fine particles, they are maintained, while in a gravel-sand mixture, they may dissipate quickly.

Three models have recently been proposed to connect the evolution of excess pore pressure with other flow dynamics. *Kowalski and McElwaine* [2013] presented a two-phase flow model that they demonstrated could be used to predict the evolution of depth-averaged particle concentration and associated pore pressure

variations. In their dynamic representation of the resuspension and sedimentation of solid particles they account for the transfer of hydrostatic pressure between the fluid phase and particle phase: from particle contacts to the fluid pore pressure during the suspension process,and back to the particle contacts as they settle. *Iverson and George* [2014] proposed a debris flow model that connects pore pressure evolution with porosity changes due to changes of effective normal stress and shearing of the grain-fluid assembly, leading to contraction or dilation of the pore space. They explicitly account for sources of excess pore pressure and dissipation of pore pressure in an independent equation. In their model, both particle network contraction and increases in the effective normal stress lead to increases in fluid pressure. Similarly, decreases in effective normal stress leads to decreases in fluid pressure. Mangeney and colleagues [e.g., *Bouchut et al*., 2015] proposed a two-phase model that allows the separation between the fluid and the solid phase free surface to make it possible for the fluid to be sucked or expelled from the solid phase due to dilatation/compression effects. Subsequently, the change in space and time of the excess pore fluid pressure and its coupling with the solid phase arises directly from the momentum conservation equations. While these are compelling models, more data are needed to understand the effect of grain size distribution on pore pressure generation and dissipation to fully capture these dynamics for a range of natural flows.

1.4. Evidence for the Influence of Grain Size Distribution on Excess Pore Pressures

Field evidence for excess pore pressures reported for natural debris flow events [*Berti et al*., 1999; *Berti and Simoni*, 2005; *McArdell et al*., 2007; *McCoy et al*., 2010, 2012] are suggestive of a grain size dependence of the phenomenology. *McArdell et al*. [2007] measured total stresses and pore pressures at the base of a debris flow in an instrumented channel in the Illgraben catchment in southwestern Switzerland. In doing so, they were able to determine what proportion of the total flow weight was supported by pore fluid pressures. Notably, at the tail of the observed debris flow, which showed a lower concentration of large clasts, total normal stress equaled to pore fluid pressure, illustrating that the flow was fully liquefied (LR = 1 in equation (4)). *McCoy et al*. [2010] found that fluid pressures toward the middle and back of natural debris flows were approximately 1.5 to 2 times the hydrostatic pressures estimated solely from the density of the interstitial fluid. In contrast, both *McArdell et al*. [2007] and *McCoy et al*. [2010] found that the increase in pore fluid pressure over hydrostatic pressure was relatively insignificant at the front of the flows, which were generally coarser grained and fluid starved.

In related experimental and computational studies, there is evidence that the variation of pore pressures and other stresses in the flow are dependent on particle size distribution in a debris flow. Simulations have shown that bulk stresses are mediated by the particle size distribution in dry granular flows [e.g., *Rognon et al*., 2007; *Yohannes and Hill*, 2010; *Hill and Yohannes*, 2011; *Tripathi and Khakhar*, 2011], which experimental data indicate extend to debris flows as well [e.g., *Hsu*, 2010]. Measurements of normal stress and fluid pressure in large-scale experiments indicate that the presence and quantity of fine particles can significantly influence the magnitude of pore fluid pressure [*Major and Iverson*, 1999; *Iverson et al*., 2010; *Kaitna et al*., 2014]. The segregation of particles during transport makes measurements to connect grain size distributions to pore fluid pressure more uncertain [e.g., *Hsu*, 2010; *Johnson et al*., 2012; *Yohannes et al*., 2012].

As indicated above, an understanding of how particle size distribution influences the formation and dissipation of excess pore pressure in debris flows is important for improving our overall understanding of debris flow processes. Pore pressure influences the entrainment of bed material by debris flows [*Berger et al*., 2010; *McCoy et al*., 2012; *Iverson et al*., 2011] with demonstrated influence on speed and runout distances [*Mangeney et al*., 2010; *Farin et al*., 2014]. *Kaitna et al*. [2014] used novel measurement techniques and demonstrated that measured velocity profiles of experimental debris flows vary with evolution of fluid pressure. Gradients in stresses themselves have been shown to segregate the particles within a mixture [*Fan and Hill*, 2011; *Hill and Tan*, 2014]. However, systematic data on how the evolution of pore fluid pressure depends on material composition in a debris flow are not yet available.

Here we investigate how mixture composition, fluid pressures relative to hydrostatic conditions, and flow dynamics are linked. We hypothesize that poor sorting in different grain size distributions leads to internal stress states (via excess pore fluid pressure) that strongly influence flow behavior. To isolate the effects of sorting and mud content at a large scale, we conducted six experiments using different particle-fluid mixtures sheared in a 4 m rotating drum, in which grain size distribution among the coarser particles (>2 mm) and the content of fine particles (<2 mm) were varied. We use several measures to identify

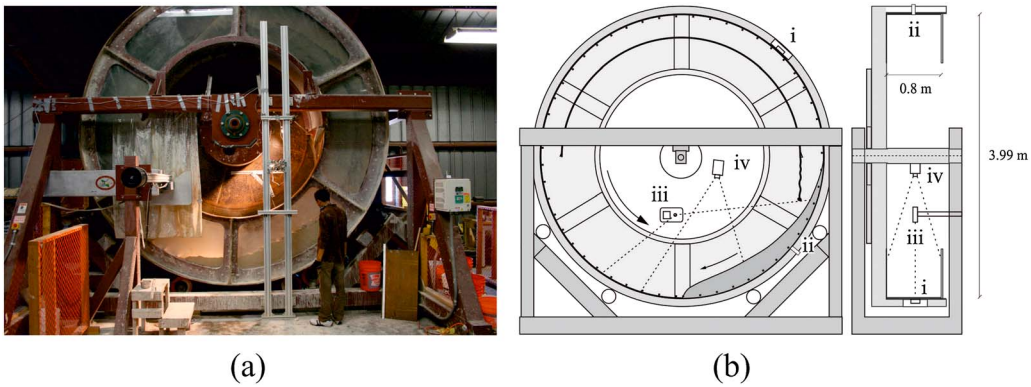

Figure 1. (a) Photo of the rotating drum and (b) functional sketch of the experimental setup showing the locations of the (i) load cell, the (ii) fluid pressure sensor, the (iii) 2-D rotational laser scanner, and (iv) digital video camera [modified after *Schneider et al.*, 2011].

differences between the flows: (1) basal fluid pressure (magnitude relative to solid normal load and to hydrostatic pressure), (2) fluctuation magnitudes of basal fluid pressure, (3) average steady state surface slope, (4) velocity and pressure distribution within the flows, and (5) dissipation of basal fluid pressure after stopping the drum. Our data suggest that we can define the transition from "muddy behavior" to "granular behavior" associated with specific grain size distributions by documenting enduring excess pore pressures in the flows and their effect on the relationships between shear and normal stresses.

2. Methods

2.1. Experimental Setup

To generate experimental sediment fluid flows, we use a large 4 m diameter, 0.8 m wide, vertically rotating drum. The use of a rotating drum allows us to develop reproducible steady state flows where profiles of velocity and fluid pressure, surface slope, and normal load are relatively easy to measure (Figure 1). The large size of the drum allows us to use material mixtures similar to those found in the field and by that to minimize scaling bias when drawing conclusions from these experiments with regard to natural flows. On the other hand, compared with a typical debris flow, the flow of particles and fluids in a drum is highly nonuniform, and we have to exercise care in considering the influence of nonuniformity of the flow and bed curvature in the interpretation of our results.

The drum has a maximum angular velocity of 1.5 radians/s, which corresponds to a drum bed velocity of 3 m/s. In this study we performed experiments at several drum speeds, with drum bed velocities varying from 0.6 m/s to 1.9 m/s but focus most of our discussion on runs where the bed velocity = 1.25 m/s. At steady state, a mixture sheared by the drum bed was essentially stationary in the laboratory frame, and the drum bed velocity was equal to the average velocity of the material relative to the drum bed (V_m).

Rubber treads with a cross section of 25 mm × 25 mm span the width of the drum, spaced ~0.2 m apart along the circumference of the drum to prevent the entire mass from sliding along the inner surface of the bed as the drum rotates. The two sidewalls are smooth; the back wall is made of steel, and the front is made of Plexiglas to facilitate measurements from one side of the flow. Additional technical details of the setup are described elsewhere [see *Hsu*, 2010; *Schneider et al.*, 2011; *Yohannes et al.*, 2012; *Hsu et al.*, 2014; *Kaitna et al.*, 2014]. For each experiment, we place a mixture of particles and fluid into the drum, rotate the drum, and monitor the resulting flow dynamics.

2.2. Material

To separately assess the effect of grain size distribution and the content of fine particles, we performed a number of experiments using six different mixtures in which we varied the coarse particle size distribution and the amount of fine particles. The mixtures we used are based on a debris flow mixture representative of a documented flow event in Taiwan [*Chen et al.*, 2001] which had a wide grain size distribution (GSD) and a high fraction of fine particles. According to *Chen et al.* [2001], in the Taiwanese debris flow the volumetric sediment

Table 1. Material Composition of the Tested Mixtures[a]

	Wide GSD + Fines	Wide GSD + Water	d_{50} + Fines	d_{50} + ½ Fines	d_{50} + ¼ Fines	d_{50} + Water
m_b (kg)[b]	1050	904	804	726	696	667
m_c (kg)[b]	727	727	533	533	533	533
m_f (kg)[b]	229	0	188	94	47	0
m_w (kg)[b]	91	177	83	99	116	134
V_b (m^3)[c]	0.452	0.451	0.355	0.336	0.335	0.335
V_c (m^3)[c]	0.274	0.274	0.201	0.201	0.201	0.201
V_f (m^3)[c]	0.087	0	0.071	0.035	0.018	0
V_w (m^3)[c]	0.091	0.177	0.083	0.099	0.116	0.134
$C_{v,f}$ (-)[d]	0.49	0.00	0.46	0.26	0.13	0.00
$C_{v,c}$ (-)[d]	0.61	0.61	0.57	0.60	0.60	0.60
$C_{v,b}$ (-)[d]	0.80	0.61	0.77	0.70	0.65	0.60
ρ_s (kg/m^3)[e]	1804	1000	1760	1435	1219	1000
ρ_b (kg/m^3)[e]	2318	2003	2264	2163	2078	1990
d_{50} (mm)[e]	10	10	10	10	10	10

[a] m = mass, V = volume, C_v = volumetric sediment concentration[d], ρ = density, and d_{50} = 50th percentile of grain diameter of the coarse fraction; subscripts *c*, *f*, *w*, *s*, and *b* denote "coarse," "fines," "water," "suspension" (i.e., interstitial fluid), and "bulk," respectively.
[b] Masses for the components reported were measured before the experiment; $m_b = m_f + m_c + m_w$.
[c] Volumes reported for the sediment are representative of the total solid volume, i.e., $V_c \cong m_c/(2650 \ \ kg/m^3)$ and $V_f \cong m_f/(2650 \ \ kg/m^3)$; volume of water was estimated according to $V_w \cong m_w/(1000 \ \ kg/m^3)$. $V_b = V_f + V_c + V_w$.
[d] $C_{v,f} = V_f/(V_f + V_w)$; $C_{v,c} = V_f/V$; and $C_{v,b} = (V_f + V_C)/V$.
[e] $\rho_s = (m_f + m_w)/(V_f + V_w)$; $\rho_b = m_b/V_b$.

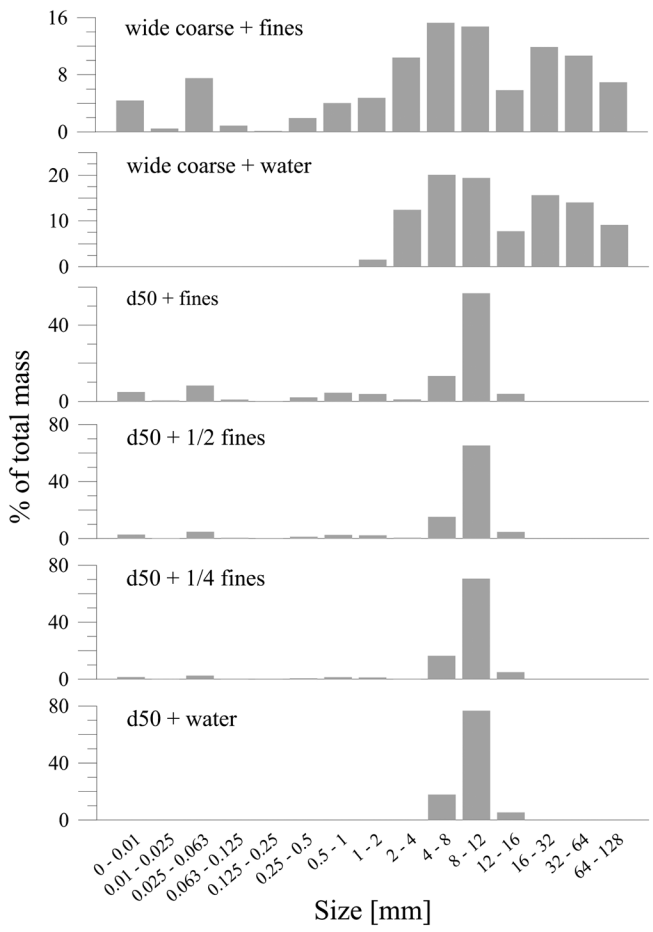

Figure 2. Histograms of the size fractions of the tested mixtures.

concentration relative to the entire mixture $C_{v,b} \approx 0.8$; the volumetric concentration of coarse particles $C_{v,c} \approx 0.61$, and the volumetric concentration of fine particles in the (muddy) interstitial fluid (the fine sediment water slurry) $C_{v,f} \approx 0.49$. We refer to the mixture we used that most closely resembled the Taiwanese flow event as "wide GSD + fines" (Table 1). Approximately 80% of our wide GSD + fines mixture by volume consisted of particles. Approximately three fourths (76% by volume, as determined by mass) of those were coarse particles (so that $C_{v,c} \approx 0.8 \times 0.76 = 0.61$). The GSD of the coarse particles of our wide GSD + fines mixture (>2 mm) was nearly identical to that of the Taiwanese flow, but we capped the maximum size of our mixture at 128 mm because of concern about damage to sensor probes that we describe shortly. The rest of the particles in our wide GSD + fines mixture consisted of fine particles, so that $C_{v,f} \approx 0.49$, The fines were primarily silt and clay, though there was a nonnegligible quantity of larger fine particles (still < 2 mm) as evident in Figure 2. The density of the interstitial fluid considering the mass and volume of the fine particles and fluid together (assuming all particles up to

2 mm are suspended) was $\rho_s \approx 1804\,\mathrm{kg/m^3}$ and total bulk density ρ_b was $2318\,\mathrm{kg/m^3}$ (see Table 1). The other mixtures we used are variations of the wide GSD + fines, achieved by systematically varying the water content and the concentration of fine particles or by replacing the coarse fraction of the wide GSD distribution with a very narrow distribution about its median grain size ($d_{50} = 10$ mm), as listed in Table 1. The grain size distributions of all the experimental runs are shown in Figure 2.

We distinguish between the "fine fraction" and the "coarse fraction" using a threshold grain size of 2 mm. This choice is arbitrary, but the definition of a threshold helps us to (1) account for the effect of turbulence and hindered settling (as we detail in section 4) and (2) to provide for an efficient use of our fluid pressure sensors whose pore spaces are approximately 2 mm (as we detail in section 2.3). In our sheared grain-fluid mixtures composed of coarse sediment, fine sediment, and water, we use the term "fluid" for the mixture of fine sediment (e.g., <2 mm in diameter) suspended in water.

The rheology of our most fines-rich interstitial fluid ($C_{v,f} \approx 0.49$) was documented using a cone plate rheometer (model Haake Rheoscope1). The response of the fluid under steady shear at strain rates, $\dot{\gamma}$, varied from 10^{-4} to $10\,\mathrm{s^{-1}}$. The fluid was shear thinning, and the data were well fit using a Herschel-Bulkley model (equation (1)). The yield strength, $\tau_y \approx 5$ Pa, the consistency index, $k \approx 8$, and the power law exponent, $n \approx 0.35$. Details of these measurements can be found in *Palucis* [2014].

2.3. Instrumentation and Measurements

We measured the longitudinal depth profile for each flow using a 2-D rotational laser scanner (model Acuity AR4000) located approximately 1 m above the flow surface (Figure 1b, iv). The scanner produced five topographic profiles per second, and we recorded these profiles over a period of 60 s for each experiment. The resulting 300 profiles were averaged to reduce error associated with the laser scatter. Vertical resolution of the average flow profile was typically ±2 mm [*Hsu et al*., 2014].

We calculated longitudinal profiles of the total normal stress using force data from a square load plate that is 15 cm × 15 cm and installed at the centerline of the flume (Figure 1b, iii). The load cell holding the plate (Model SWP10-5 KB000 precision force transducer by Interforce Inc.) has a capacity of 22 kN. As the sensor passes beneath a sheared mixture, it measures the magnitude of the normal force as it varies along the length of the flow. The normal stress was set equal to measured force divided by the area of the plate (after subtracting out effects such as centripetal force and the weight of the plate). Typically, we recorded three such sets of longitudinal measurements (corresponding to three drum rotations) per experiment at each velocity.

We measured longitudinal profiles of basal fluid pressure using a fluid pressure sensor installed at the center of the flume bottom approximately 90° upstream of the load plate (Figure 1b, ii). The pressure transducer (Keller Inc., model PR-25Y with a nominal pressure range between −0.1 and 0.1 bar) is attached to a closed reservoir filled with oil (Figure 3). A closed system was used because the sensor is turned upside down through each rotation of the drum. To close the system, we sealed the open end that is in contact with the fluid with a flexible membrane overlaid by a steel mesh. The mesh size is 2 mm and prevents impacts onto the membrane by particles larger than 2 mm. Because the mesh size was still relatively large, fluid pressure was rapidly transmitted onto the membrane and, via the closed oil reservoir, to the pressure transducer. Expansion and contraction of the oil due to temperature changes could have a direct impact on the measured pressures, i.e., a slow drift of the pressure value representing atmospheric pressure. To account for this, we measured the atmospheric pressure during the portion of each drum rotation when the pressure sensor was not in contact with the flow and calibrated the pressure signal for each rotation using these data. The relatively large mesh size, which allowed for more responsive pressure measurements, caused particles up to 2 mm to be included as part of the fluid weight that drove pore pressure.

Additionally, we recorded the variation (typically, the decay) of basal fluid pressure after the drum stopped rotating (with the basal pressure sensor at the six o'clock position). Because the measurement device for fluid pressure is a closed system, minor temperature changes and subsequent density changes of the oil in the pressure sensor gave rise to anomalous pressure drift, so we restricted the length of these static measurements to 5 min (300 s).

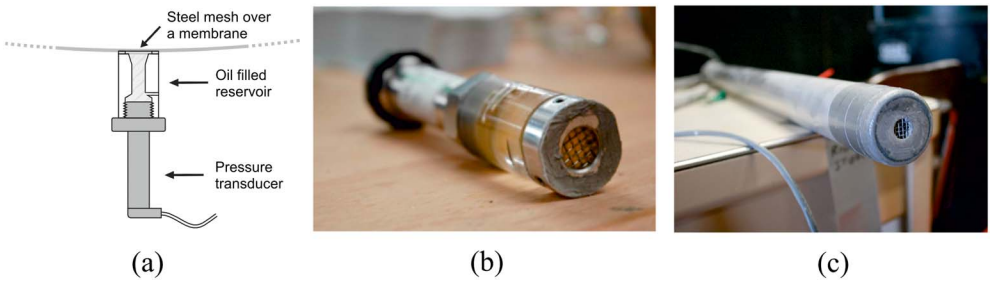

Figure 3. (a) Sketch of the configuration of pressure sensors for experiments in a rotating drum, (b) photo of the basal sensor before installation, and (c) miniaturized pressure sensor installed into a steel tube to be immersed into the flow.

For selected experimental runs we also used a novel fluid pressure sensor probe and a velocity profilometer that we placed at different flow depths, to obtain a vertical profile of fluid pressure and velocity at specific locations in the flow. We performed these measurements in the deepest part of each flow. The pressure sensor probe is similar to the fixed boundary pressure sensor described above (Figures 3a and 3b) but employs a miniaturized transducer (Keller Inc., model PAA-9-FLY, with a nominal pressure of 800–1300 mbar, dimensions 30 mm diameter × 60 mm long). We installed the sensor at the tip of a steel tube with an outer diameter of 35 mm (Figure 3c). During each experiment we lowered the sensor into the flow in a stepwise fashion and collected measurements at a frequency of 1 kHz for 30 s at several discrete depths in the flow. As we discuss shortly, because of the potential influences of the presence of the sensor assembly, the measured pressure profiles are likely not exactly equal to those in undisturbed flow, but we use this information to determine how these pressure profiles vary with changes in particle size distribution. As is true of the pressure sensor in the drum bed, temperature changes within the oil reservoir of the pore pressure probe may also affect the signal. To minimize this effect in our data, we recorded the atmospheric pressure reading before and after each set of pressure measurements. We found that the change in this baseline pressure was minimal for each experiment: the maximum variation (standard deviation) between the measured atmospheric pressures over the course of each experiment was 260 Pa, corresponding to approximately 5 to 10% of the expected maximum hydrostatic fluid pressure in our experiments (i.e., 26 mm of water).

The velocity profilometer is composed primarily of two conductivity probes mounted on the tip of a rod (similar to the assembly that houses the pressure sensor) a small distance, s, apart from one another. We immerse the rod in the flow so that one conductivity probe is located downstream of the other. For each depth into the flow, we recorded conductivity measured by each probe at a frequency of 1 kHz for 40 s so that the measured conductivities of the two probes are similar but with a slight time delay Δt determined through cross correlation of similar conductivity signals. This delay can then be used to calculate the local mean velocity using $v = s/\Delta t$. This method, which is similar to velocity measurements in granular flows [*Ahn et al.*, 1991; *Louge et al.*, 1996] and snow avalanches [*Kern et al.*, 2004], is described in detail by *Kaitna et al.* [2014]. Because of concerns over the bigger cobble-sized particles damaging the probe, for some mixtures we inserted the probe only partway into the flow and therefore our fluid pressure measurements were restricted to the upper half of the flow.

2.4. Data Acquisition and Analysis of Pore Pressure and Normal Stress at the Bed

The load cell and fluid pressure sensors were sampled at 50,000 Hz, and every 50 data points were averaged so that the data were recorded at an effective sampling rate of 1000 Hz (e.g., Figure 4). We performed several steps to eliminate spurious components in the time series of our measurements signals. Measurements were made while rotating the empty drum to determine significant contributions to frequencies associated with machine noise (e.g., vibrational response of the drum). These frequencies ranged between 7.5 and 25 Hz, and therefore, a stop-band filter was used to exclude these frequencies from our raw data of the pressure and normal stress sensors. The resonant frequencies of the load cell (from 190 to 200 Hz) and of the panels that carried the fluid pressure sensors (from 100 to 140 Hz) were revealed by hitting the load plate and the panels with a hammer while recording the pressure signal. The characteristic frequencies of these devices ranged between 100 to 140 Hz for the load cell and 190 to 200 Hz for the pressure sensors. Consequently,

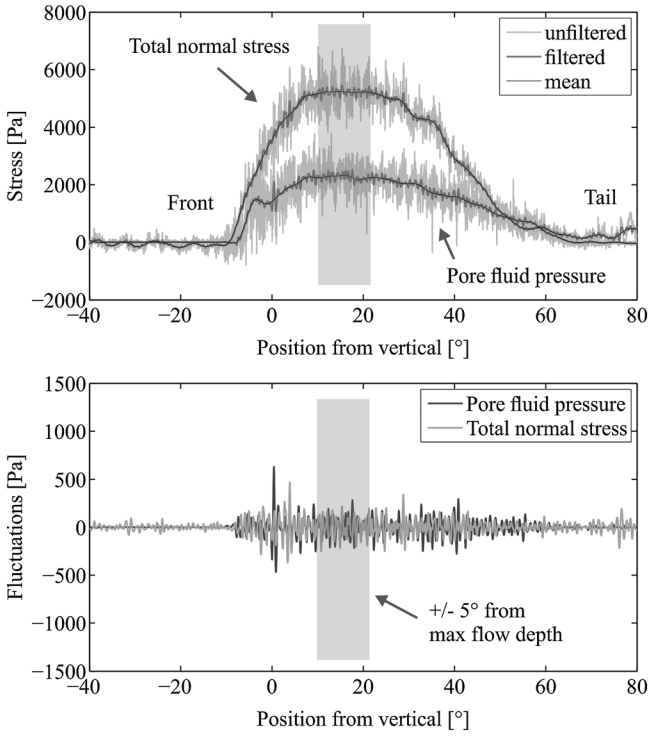

Figure 4. (top) Time series of basal fluid pressure and total normal stress. This example shows mixture d_{50} + water at a mean rotation velocity of $v_m = 1.25$ m/s. Figure 4 (top) shows the time series before and after filtering as well as (bottom) the mean time series which is subtracted to derive fluctuations around the mean. The grey shaded area indicates the region of ±5° from maximum flow depth which was used to calculate respective average values.

the signal was low-pass filtered at 50 Hz. The average normal stress profiles were calculated from the filtered data averaged over an arc length of 1° and over three consecutive rotations. The error bars presented in this study (e.g., those in Figure 7) were calculated using the standard deviation of the mean over the same 1° arc length for three consecutive rotations.

As a measure of the fluctuating component of normal stress and fluid pressure we used the time series of the signals, filtered, as described above, and subtracted from these the same filtered time series, a low-pass-filtered time series at 10 Hz. The resulting time series of fluctuations (e.g., Figure 4) therefore effectively represents the original time series, filtered to contain frequencies between 25 Hz and 50 Hz. These measurements do not necessarily represent the true stress and fluid pressure fluctuations at the particle scale. For example, there might be fluctuations at frequencies that were filtered out, or at length scales smaller than the relevant dimensions of the measurement devices. We therefore use these measures to provide systematic indicators of quantitative differences in stresses from one sediment fluid system to the next rather than absolute measures of the stresses for each experiment.

Several components contribute to the total fluid pressure in a situation where an elevated fluid pressure P_e may be relevant (Figure 5). For simplicity, we assume uniform fine sediment concentration and a linear vertical pressure profile. These assumptions lead to equation (6) as a means to calculate hydrostatic pore pressure for water, P_w, with a density ρ_w:

$$P_w = \rho_w g(H - z)\cos\theta, \tag{6}$$

The additional component to hydrostatic fluid pressure due to the fine sediment in suspension, P_s, is

$$P_s = (\rho_s - \rho_w)g(H - z)\cos\theta, \tag{7}$$

Because of the dimensions of the pore pressure sensor, we must include all fine particles up to 2 mm in diameter in the calculation of ρ_s (see footnotes to Table 1).

In addition to the fluid hydrostatic pressure measured at the bed, there are two other factors contributing to the total fluid pressure and normal stress at the bed. First, there is the centripetal force associated with flow in our curved channel bed. In this study we kept the drum speed relatively low so that the effect of centripetal acceleration on the measured values of pore pressure are relatively low [cf. *Hsu*, 2010]. To estimate this effect, consider the flow at each distance from the drum center R_i as having a velocity v_i along circular flow lines with radii of curvature R_i. Our independent measure of the vertical velocity profile $v(z)$ can be used to estimate the contribution of centripetal acceleration to fluid pressure, P_{ca}, for n discrete layers of equal thickness H_i with

$$P_{ca} = \sum_{n}^{i=1} \rho_s \left(v_i^2 / R_i\right) H_i \tag{8}$$

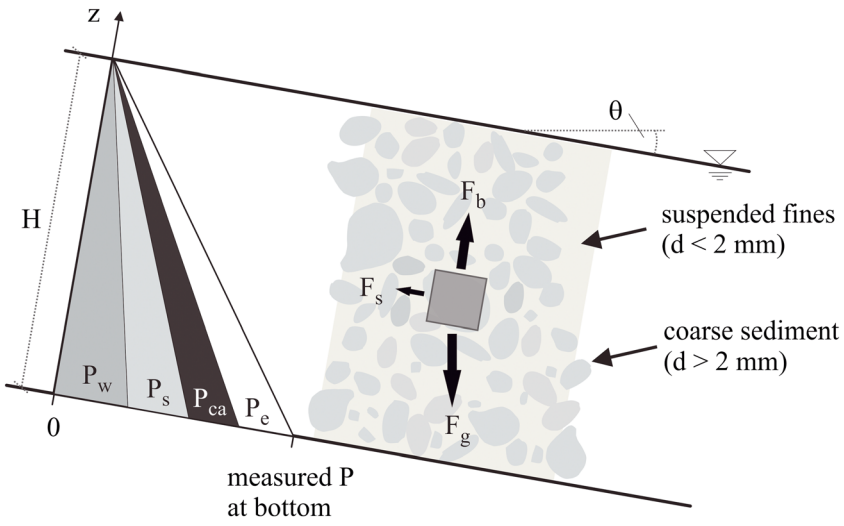

Figure 5. Illustrations of (left) the different components contributing to the total fluid pressure (not to scale) and (right) forces acting on a suspended sediment grain (F_b = buoyancy force, F_g = gravity force, and F_s = shear force. V = volume of the suspended particle). The different pressure components are defined in the text in equations (6)–(9).

Finally, excess fluid pressure, P_e, which cannot be explained by the buoyancy of water, suspended fines, or by centripetal acceleration, may be calculated from the other pressure terms, where P is the pressure measured by the sensor at the base of the drum

$$P_e = P - P_w - P_s - P_{ca} \tag{9}$$

3. Results

For all mixtures, steady flow developed after several rotations of the drum with a distinct front that was steeper than the main body of the flows. Visual observations and pressure measurements indicated that some degree of solid-fluid segregation in each flow, which suggests disparate fluid and particle velocities at least in some regions of the flow. Solid-fluid segregation was velocity and mixture dependent. At high drum velocities an unsaturated region grew at the front, and fluid was pulled backward away from the direction of flow; at low drum velocities, fluid drained from the front, so that the fluid front preceded the granular front similar to that described in *Kaitna et al.* [2011] and *Leonardi et al.* [2015]. This latter effect was more pronounced for the mixtures that contained few or no fine particles and for the mixtures where the GSD of the coarse fraction was narrow. For most of the flows at a constant speed of 1.25 m/s presented here, the front was fully saturated and the front of the fluid meets the front of the granular materials (Figure 6b). For the wide coarse + water mixture the front was primarily liquid, and the interstitial fluid front preceded the granular front (Figure 6a). These visual observations are supported by the average normal stress and fluid pressure profiles.

3.1. Profiles of Mixture Dynamics

Figure 7 shows longitudinal profiles of the average total normal stress and fluid pressure at the flume bottom compared with profiles of theoretical basal hydrostatic fluid pressures for all six mixtures. To calculate the theoretical hydrostatic pressures, we used equations (6) and (7) with the laser scan data for the flow depth and estimated densities of the muddy pore fluid as presented in Table 1 and of the water (≈1000 kg/m^3). In both cases we assume complete saturation (i.e., pore spaces filled with fluid from the bottom of the drum to the measured flow surface). For all cases the normal stress and fluid pressures are essentially in phase with the flow depth (represented by the hydrostatic pressure plots in Figure 7). Local deviations for individual runs indicate important influences of grain size distributions and the presence of fines in these mixtures with two exceptions. First, just after the front of the flow, there is a small peak in the fluid pressure before the bigger peak associated with the main flow. We attribute this to a dynamic vertical pressure component when the material is overflowing the roughness elements. Additionally, for some mixtures, measured fluid pressure exceeds total normal stress at the tail of the flow between locations 40 and 50° from vertical. We do not

Figure 6. Overview looking downslope of mixtures (a) wide coarse + water, having an oversaturated front, and (b) the d_{50} + water mixture, having a saturated to slightly unsaturated front. Figure 6b was observed for all other tested mixtures.

attribute this to a slow response of the sensor during pressure decay, but to anomalous effects associated with the drum geometry at high angles and the fact that fluid might get trapped behind roughness elements. In the immediate vicinity of the load plate, practical limitations required the removal of some of the roughness elements, explaining why these two effects are not evident in the profiles for the normal stress.

Figure 7a shows that for the natural debris flow mixture (wide GSD + fines) the measured fluid pressure significantly exceeds both theoretical hydrostatic pressures (those calculated with and without consideration of suspended fines), over nearly the complete length of the flow (i.e., excess fluid pressure prevails). Hence, fluid pressure is a significant fraction of the total normal stress, and LR is close to 1, indicating that a fraction of the coarse particles must effectively be supported by the fluid rather than by grain-to-grain contacts over a long period of time. This reduces frictional grain-grain contacts [*Kaitna et al*., 2014], and correspondingly, the steady state position of the flow is the farthest forward in the drum for all mixtures, as one would expect from reduced frictional resistance of the flow.

Figure 7b shows that when the mixture is composed of the same coarse grain size distribution as the natural debris flows, but the fine fraction is replaced by water (wide GSD + water), the fluid pressure equals hydrostatic through much of the flow. This indicates that the frictional particle-particle contacts are greater compared with the first case with the high percentage of fine particles. Correspondingly, relative to the first mixture, the entire debris flow is shifted upslope (to the right in Figure 7b) as one would expect from increased frictional resistance of the flow. In contrast with the rest of the flow, for this mixture the pore pressure exceeds estimated hydrostatic pressure at the flow front. There is also a solid-fluid segregation at the flow front that gives rise to a fluid bore preceding the debris (Figures 6a and 7b). In this region particles enter into the fluid front from the top of the solid front immediately behind this region, then segregate from the fluid into eddies at the sides of the front and circulate in concentrated patches before being dragged back into the flow at depth.

Figure 7c presents data for the case where the amount of fines remains unaltered compared to the original mixture but the entire distribution of the coarse fraction is replaced by the sediment close to the d_{50} of the coarse fraction (d_{50} + fines). As in the case with a broad GSD, excess fluid pressure develops under much of the flow, but the excess is smaller and, toward the front of the flow (from approximately −10° to +10°), there is no excess; that is, the measured basal fluid pressure does not exceed calculated hydrostatic fluid pressures associated with the interstitial (muddy) fluid. The flow is not shifted forward in the drum, and the magnitude of the total normal stress and fluid pressure is much less than the wide GSD case. This provides a strong indication that in addition to the presence of fines, a wide GSD is a key component for the presence of excess fluid pressure over long timescales.

The profiles for the mixtures d_{50} + ½ fines and d_{50} + ¼ fines in Figures 7d and 7e, respectively, are similar to those for d_{50} + fines with one exception. In these mixtures the measured fluid pressures were slightly below a

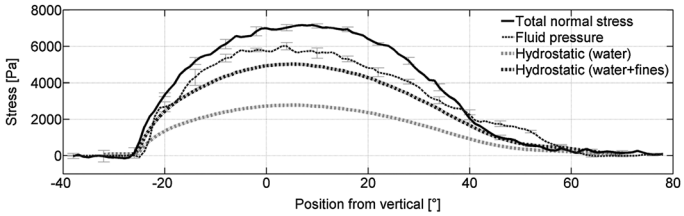

(a) *wide GSD + fines*

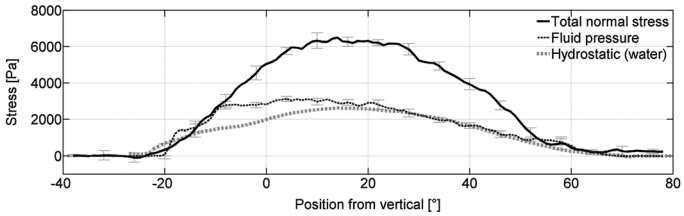

(b) *wide GSD + water*

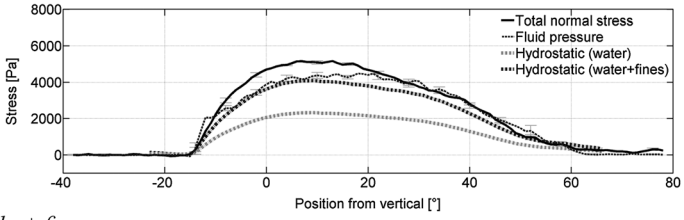

(c) d_{50} + *fines*

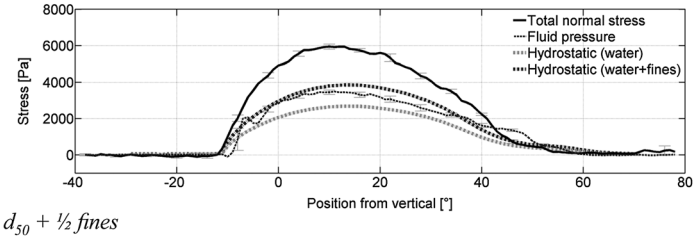

(d) d_{50} + ½ *fines*

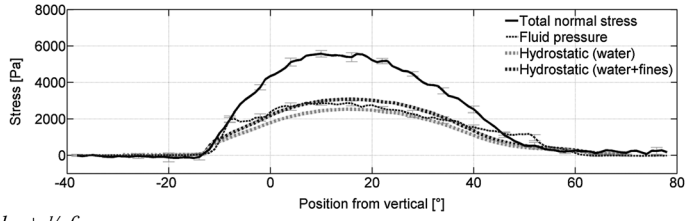

(e) d_{50} + ¼ *fines*

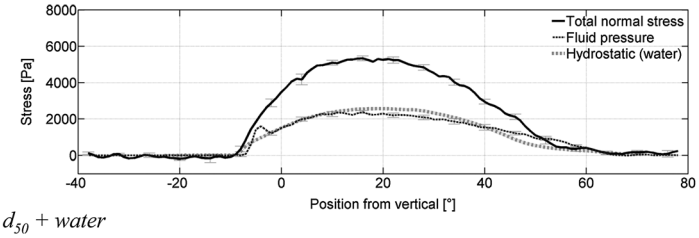

(f) d_{50} + *water*

Figure 7. Longitudinal profiles of the averaged measured normal stress and fluid pressure and the calculated hydrostatic fluid pressures at the base, using longitudinal flow depth measurements and estimated values for the interstitial fluids ("water + fines" in Table 1) and water (≈1000 kg/m^3). Data plotted for (a) wide coarse + fines, (b) wide coarse + water, (c) d_{50} + fines, (d) d_{50} + ½ fines, (e) d_{50} + ¼ fines, and (f) d_{50} + water at a mean flow velocity of 1.25 m/s. The abscissa represents the angular distance from the vertical, i.e., zero corresponds to the six o'clock position; positive angles correspond to positions upstream or toward the tail of the flow.

Table 2. Measured Basal Mean Normal Stress σ_{tot} and Pore Fluid Pressure P at the Deepest Part of the Flow at a Mean Velocity of 1.25 m/s; Mean Theoretical Fluid Pressures (Based on Height Measurements, Velocity Measurements, Estimated Densities From Table 1, and Equations (6)–(9) and Pressure Ratios

	Measured (Pa)		Calculated[a] (Pa)				Pressure Ratios (-)			Surface Slope	Diffusion Coefficient[f]
Mixture	σ_{tot}	P	P_w	P_w+P_s	P_{ca}	P_e	LR[c]	$\widetilde{P}_{e,max}$[d]	$\widetilde{P}_{e,min}$[e]	θ (deg)	D (m^2/s)
Wide GSD + fines	7075	5766	2749	4959	112	695	0.82	2.10	1.16	7.7	1.5×10^{-6}
Wide GSD + water	6076	2964	2639	2639	100[a]	231	0.49	1.12		22.5	1×10^{-4}
d_{50} + fines	5096	4308	2296	4042	100[b]	166	0.85	1.88	1.06	17.5	4×10^{-6}
d_{50} + ½ fines	5849	3410	2645	3796	100[b]	-	0.58	1.29	0.90	16.7	1×10^{-5}
d_{50} + ¼ fines	5490	2795	2486	3030	88	-	0.51	1.12	0.92	18.5	7×10^{-6}
d_{50} + water	5247	2290	2526	2526	99	-	0.44	0.91		22.6	1×10^{-2}

[a] P_w, P_s, P_{ca}, and P_e are different components of measured fluid pressure P, see equations (6)–(9).
[b] Estimated values based on estimates for mixtures where velocity profiles were available.
[c] $LR = P/\sigma_{tot}$, see equation (4).
[d] Pressure ratio indicating maximum estimate of excess pore pressure for values $\widetilde{P}_{e,max} > 1$, see equation (10).
[e] Pressure ratio indicating minimum estimate of excess pore pressure for values $\widetilde{P}_{e,min} > 1$, see equation (11).
[f] Diffusion coefficients D for investigated mixtures calculated by fitting equation (12) to measured fluid pressure over 300 s after cessation of movement.

theoretical hydrostatic pressure associated with the interstitial muddy fluid, $P_w + P_s$, over most of the flow length but higher than hydrostatic with respect to P_w. These slightly lower values may result from either not all particles <2 mm being suspended or a solid-fluid segregation effect where the fluid does not completely fill the pore spaces to the top of the flow, resulting in a surface that is not saturated, as we discuss in more detail shortly (Figure 11). The latter might be true for the mixture d_{50} + water, for which measure fluid pressure is slightly below P_w (Figure 7f). The dilation of the unimodal granular mass due to shearing may contribute to this unsaturated surface layer.

In Table 2 we provide a quantitative comparison of the mean basal pressure, P, and total normal stress, σ_{tot}, for the deepest region of the flow, i.e., calculated from our measured values ±5° from maximum flow depth (grey shaded area in Figure 4). The central region is selected to minimize boundary effects at the front and tail of the flow. Three metrics of P are used to quantify the effect of pressure on the grain stresses: the first is the ratio between basal fluid pressure and total normal stress (the liquefaction ratio LR, equation (2)). As previously discussed, as LR increases, more of the weight of the particles is supported by the fluid, rather than by other grains. Our second metric is the ratio of the measured pore pressure to the pressure predicted from water alone, a minimal estimate of the contribution of the fine particles to the density of the interstitial fluid, and therefore a maximal representation of the excess pore pressure:

$$\widetilde{P}_{e,\max} = \frac{P}{P_w} \approx 1 + \frac{P_e}{P_w} + \frac{P_{ca}}{P_w} + \frac{P_s}{P_w} \tag{10}$$

Our third metric is the ratio of the measured pore pressure to the pressure predicted from the interstitial fluid assuming all particles up to 2 mm in diameter are suspended, a maximal estimate of the contribution of all fine particles to the interstitial fluid, and therefore a minimal representation of the excess pore pressure:

$$\widetilde{P}_{e,\min} = \frac{P}{P_w + P_s} \approx 1 + \frac{P_e}{P_w + P_s} + \frac{P_{ca}}{P_w + P_s} \tag{11}$$

(where $P_S = 0$ if no fines are present). Since P_{ca} is essentially the same for all mixtures, the higher $\widetilde{P}_{e,\max}$ is, the greater the effects of excess pore pressure that are not associated with an increased density associated with fine particles in the mixture.

The representative values for the ratio LR are greater than 0.80 for the two mixtures with the highest fraction of fine particles (~22% of the total weight and ~70% of the weight of the interstitial fluid for both mixtures). For the mixtures lacking fine material, and likely having an unsaturated surface layer, LR is below 0.5. Pore pressure in excess of P_w is significant for all mixtures where fine sediment is present. The results plotted in Figure 7 strongly suggest that this is at least in part because fine particles are suspended in the water, effectively increasing the density of the interstitial fluid and associated hydrostatic pressure. For the wide GSD + fines mixture, values of P_e and $P/(P_w + P_s)$ suggest that the high degree of liquefaction is associated with excess pore pressure beyond that associated with the high interstitial fluid density due to the fine particles in suspension. For the d_{50} + fines mixture, these values suggest that the high degree of liquefaction

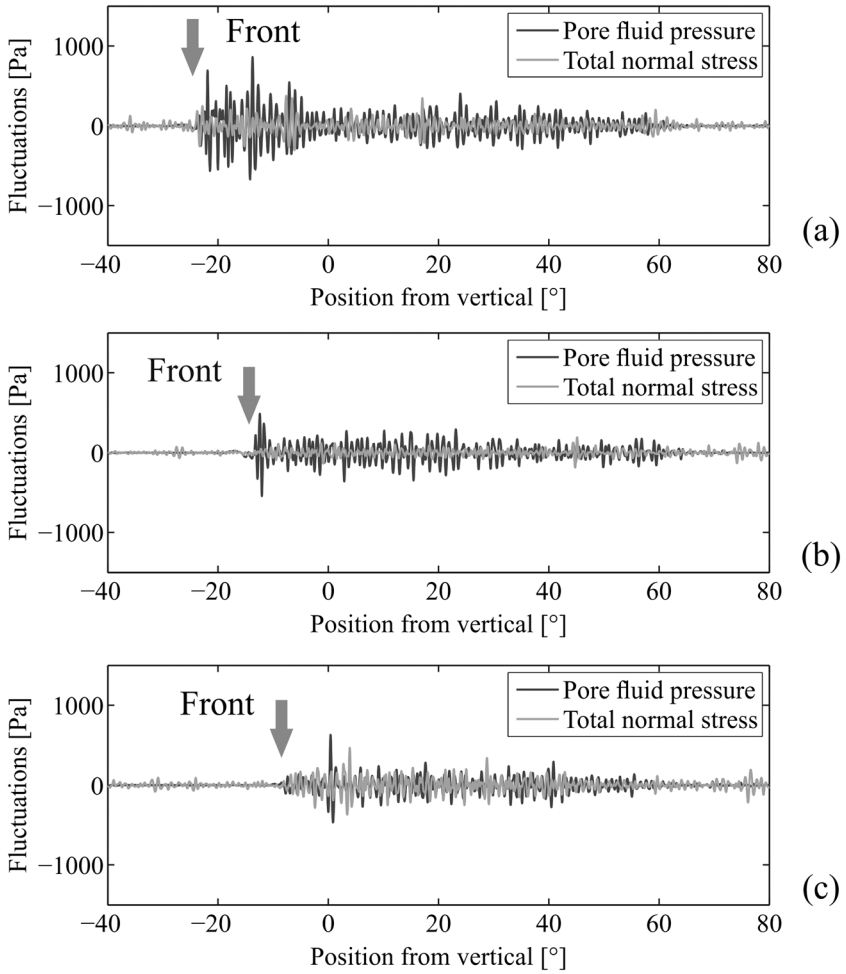

Figure 8. Fluctuating component of basal normal stress and fluid pressure for (a) wide GSD + fines, (b) d_{50} + fines, and (c) d_{50} + water at a mean flow velocity of 1.25 m/s. Signals were processed as described in section 2.

is primarily due to the higher density of the interstitial fluid associated with the fine particles. It is interesting to note that, while the excess pore pressure P_e, calculated from equation (9), is relatively large for the wide GSD + water mixture, the LR is relatively low. We discuss this more below. Finally, for all cases, the pressure associated with centripetal acceleration P_{ca} is small compared with the total measured basal pressures and stresses and is similar for all mixtures, so it likely has minimal effects on the apparent variation of LR and P_e with debris flow grain size distribution.

3.2. Fluctuations in Stress and Pressure

To consider the underlying mechanisms for excess pore pressure, we also calculate fluctuations in basal stress and fluid pressure and their correlations with changes in bulk flow resistance and other kinematics of the flow. The pressure sensor is similar in size to the median grain size of the coarse fraction of the mixtures, so fluid pressure values are effectively sampled at the particle scale. In contrast, the normal stress is derived from a load plate with an area of 225 cm^2, an order of magnitude larger than the cross-sectional area of the largest particle in the flow. Therefore, the normal stress fluctuations are smoothed over a relatively large area and cannot be directly compared to local fluid pressure fluctuations.

Figure 8 shows the complete longitudinal profile of normal stress and fluid pressure for three mixtures, demonstrating that at the front of the flow, the fluctuations are typically largest for both the normal stress and the fluid pressure. This is particularly pronounced for the unsorted mixtures shown in Figure 8a. Three factors likely contribute to greater fluctuations at the front of the flow [e.g., *Yohannes et al.*, 2012]. First, at the front of the flow, grain-grain interactions are more "collisional" and less frictional, leading to the increased

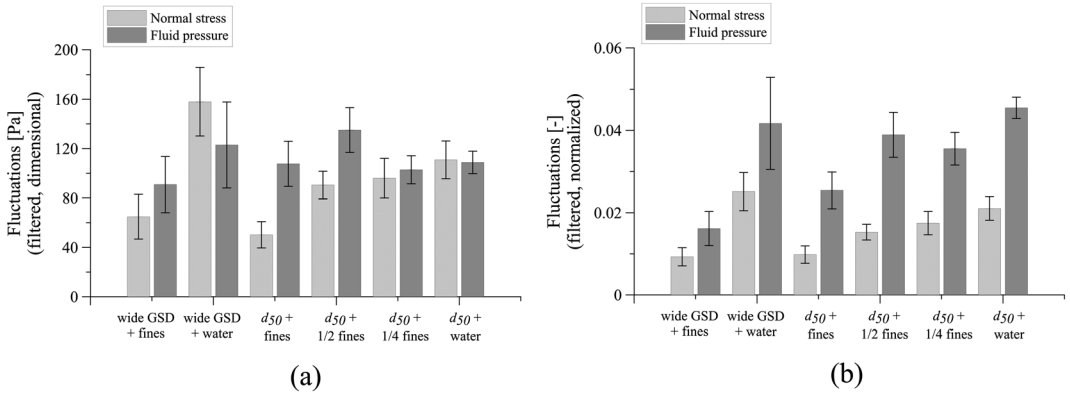

Figure 9. (a) Dimensional and (b) normalized fluctuations of normal stress and fluid pressure at the deepest section of the flow averaged over 6–12 rotations at a mean velocity of 1.25 m/s.

fluctuations for both normal stress and fluid pressure. Second, for the wide GSD mixtures, the large particles segregate to the front of the flow [e.g., *Hsu*, 2010; *Yohannes et al*., 2012]. Increased collisional dynamics associated with large particles alone also give rise to greater stress fluctuations at the bed. Third, due to the overriding motion at the front, there is necessarily a bed-normal velocity component, that may lead to higher fluctuations at the front. The data presented here show that these effects are not just limited to fluctuations in stress, as in the dry flows presented in *Yohannes et al*. [2012] but also apply to fluctuations in fluid pressures. We also note that in all three cases, high fluctuations at the front correspond to apparently high values of the liquefaction ratio at the front.

To quantify the variation of the fluctuations from one mixture to the next, we first calculate the standard deviation of the mean fluid pressure and the mean normal stress for each rotation in the particular experiment (Figure 8). For each rotation for each experiment, we calculate the average of the root mean square of each such time series data. The average and standard deviation about this average for each quantity are presented in Figure 9a for all mixtures (plotted as bars and error bars, respectively, in Figure 9). Figure 9b shows these data normalized by the average values for each mixture.

For both the wide and narrow coarse GSD, the dimensional and normalized normal stress fluctuations increased with decreasing fines content. This is in accordance with earlier work by *Hsu et al*. [2008, 2014]. The normal stress fluctuations increased slightly with broadening of the coarse grain size distribution. P_e increased both with increasing fines content and increasing coarsening of the gravel grain size distribution. On the other hand, the LR increased with increasing fines content, suggesting that as the liquid supported greater fraction of the total stress, not only did enduring contacts decrease, but collisional interactions did as well.

In contrast, fluctuations in fluid pressure do not simply vary with P_e, LR, or the fines content. This indicates that increased interparticle collisions did not necessarily correlate with increased pressure fluctuations. The stress fluctuations increased for lower fines content, and at these lower fines content the flow resistance of the interstitial fluid decreased allowing the fluid to flow more easily in response to collisional interactions and hence not become trapped.

3.3. Bulk Flow Resistance

In Figure 10 we plot the average surface slope (see also Table 2) of the flow—a measure of the bulk resistance—as a function of the liquefaction ratio for each mixture. The new data here along with similar data from experiments by *Kaitna et al*. [2014] (salient details here in Table 3) demonstrate that there is a strong relationship between LR and the average surface slope. As LR increased from zero for the unimodal 4 mm dry system to 0.8 for the wide GSD + fines mixture the mean surface slope decreased from ≈33° to 7.7°, essentially monotonically, though there is significant scatter. In general, the slope was independent of d_{50} of the coarse fraction but inversely dependent on fine particle content. Exceptions to this involve the flows with comparable values of high LR (≈ 0.8). Surface slopes for these flows varied from ≈7.7° to 17.5°. This might be connected to the high sensitivity of bulk flow resistance on the water content of the fluid (i.e., water + fines) at high liquefaction ratios or low effective normal stress, which is directly connected to frictional flow

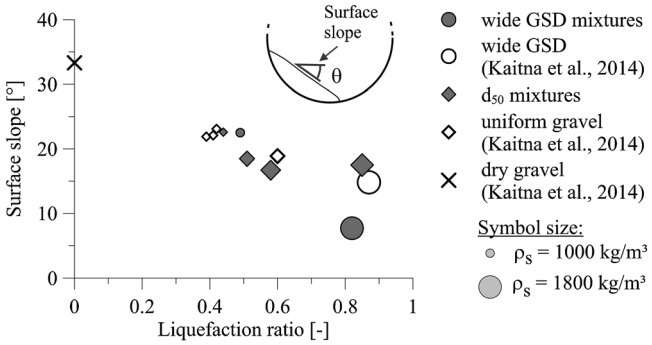

Figure 10. Relation between average surface slopes and liquefaction ratio from new data presented in this paper and from *Kaitna et al.* [2014] as indicated. The slopes are measured at the deepest point of the flow as shown in the inset.

resistance. We suspect that the d_{50} + fines run was affected by a decrease in fluid water content due to evaporation over the course of the experiment and therefore an increase of $C_{v,f}$ which is associated with an increase of fluid viscosity that might have increased bulk flow resistance.

3.4. Vertical Fluid Pressure and Velocity Profiles

For a subset of the experiments, we also measured vertical profiles of fluid pressure and velocity. These results and related measurements from the boundaries are presented in Figure 11. Velocity profiles from independent experiments with similar mixtures in the same drum (Table 3) reported by *Kaitna et al.* [2014] are included for comparison. The dashed lines represent theoretical hydrostatic pressure with respect to the density of water (calculated with equation (6)) and solid line hydrostatic pressure accounting for fines sediment (<2 mm) in suspension, calculated with equation (7).

Velocity and pressure profiles (Figures 11a and 11b) from the runs with few or no fines had similar features. Fluid pressure was insignificant between the surface and approximately 100 mm below the surface, supporting the visual observations that for these cases the upper layer of the flow was not saturated. The pressures increased linearly toward the measured basal pressure, which was somewhat less than the predicted hydrostatic value calculated assuming fully saturated conditions. The measured fluid pressure gradients are slightly shallower than those predicted using interstitial fluid densities and equations (7) and (8). The corresponding velocity profiles were slightly concave up over much of the flow depth and essentially plug-like in the upper 25% of the flow. We propose that this unsheared plug-like region was a result of reduced buoyancy and high frictional grain resistance due to reduced saturation. The velocity profile for mixture d_{50} + ¼ fines (Figure 11b) exhibited minor differences from that of the mixture d_{50} + water (Figure 11a). Specifically, the plug-like flow at the top of the velocity profile extends below the desaturated level and connects to a nearly linear velocity profile for the lower 50% of the flow depth. Data from experiments with 10 mm gravel + water [*Kaitna et al.*, 2014] also had an unsaturated top layer and a similarly shaped velocity profile (grey shaded line in Figure 11a).

We note two significant differences for the mixtures with wider coarse GSD and a higher percentage of fines (Figure 11c) that may be associated with the higher LR also associated with these mixtures. These involved the apparent degree of saturation in the pressure profile and the depth of the plug-like region of the velocity profile. The pressure data indicate that the fluid saturated the pores to the top of the mixture. Surprisingly, fluid pressure in the upper half of the flow was slightly lower than expected based on those predicted using

Table 3. Relevant Details of the Mixtures From *Kaitna et al.* [2014] Included in the Plots in Figures 10 and 11

			Uniform Gravel (2014)			
	Wide GSD+ Fines[2014]	Dry Gravel (2014)	4 mm + water	10 mm + water	13 mm + water	13 mm + mud
d_{50} (mm)[a]	8	4	4	10	13	13
m_c (kg)[b]	650	455	455	455	455	455
m_f (kg)[b,c]	242	0	0	0	0	44
m_w (kg)[b]	91	0	106	113.4	154	113.4
LR[b]	0.87	0	0.39	0.41	0.42	0.60
θ (deg)[b]	14.8	33.3	21.9	22.1	23.1	18.9

[a]The coarse particles of the wide GSD+ fines[2014] mixture were of a similar GSD to the coarse particles in our mixture except the largest particle size in the former was only 32 mm. For all other mixtures, the GSD was narrowly distributed about the d_{50} given.
[b]m = mass (subscripts *c*, *f*, and *w* denote "coarse," "fines," and "water"), LR = P/σ_{tot}, equation (4), and θ is the average surface slope.
[c]As for the mixtures presented for the first time in this paper, the mass of the fines included sizes up to 2 mm.

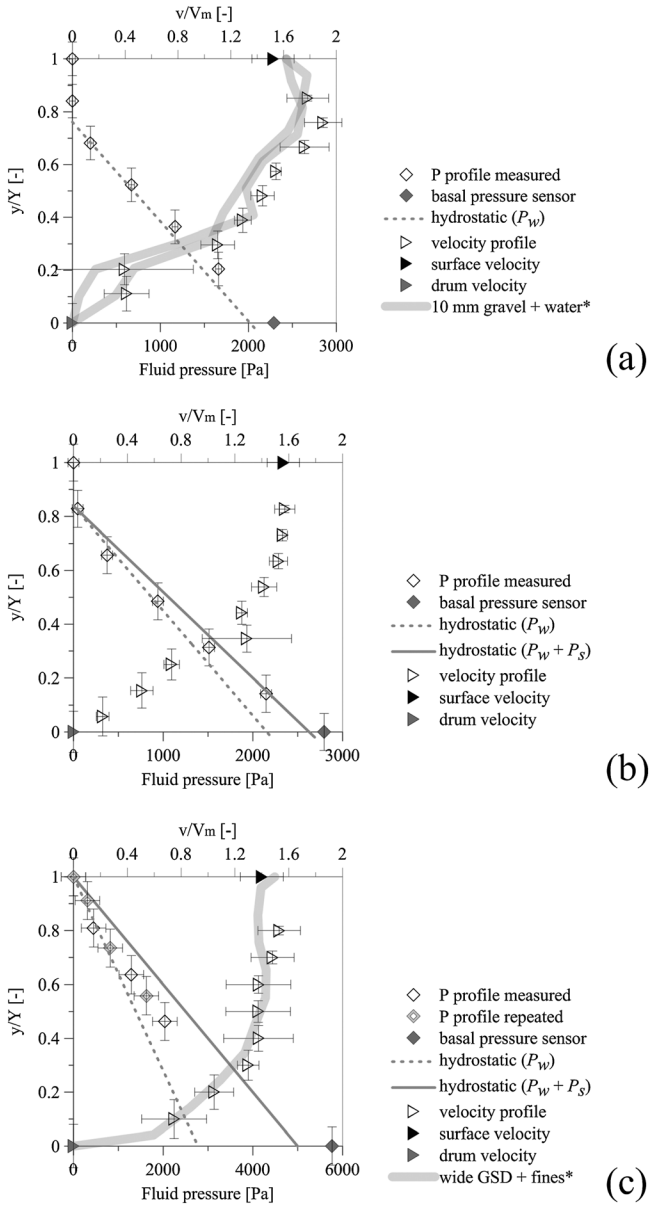

Figure 11. Vertical profiles of fluid pressure (diamonds) and particle velocity (triangles) for mixtures (a) d_{50} + water, (b) d_{50} + ¼ fines, and (c) wide GSD + fines at a mean velocity of 1.25 m/s. All data were measured using the velocity and pressure probes except those at the boundaries, which were measured using the sensor at the drum bed, atmospheric pressure, tangential drum speed, and surface velocity derived from particle tracing. Error bars for measured fluid pressure represent the standard deviation of repeated reference measurements of atmospheric pressure. Error bars for velocity represent the standard deviation of eight subsequent velocity measurements of 40 s each. Dashed line represents theoretical hydrostatic pressure with respect to the density of water (calculated with equation (6)) and solid line accounting for fines sediment (<2 mm) in suspension (calculated with equation (7)), based on assumption outlined in the text. Bold lines marked with an asterisk in the legend represent similar experiments in the same configuration presented by *Kaitna et al.* [2014].

interstitial muddy fluid density and equation (8), while the basal fluid pressure exceeded the predicted pressure. The velocity profile is nearly the same as that reported by *Kaitna et al.* [2014] for a similar mixture. For both cases, the plug-like conditions extend through the upper half of the flow profiles and the near-bed shear region is much higher.

3.5. Static Pressure Dissipation

In Figure 12, the first 5 min of basal fluid pressure immediately after the drum stopped rotating are shown for each experiment. The plotted curves are normalized by the theoretical hydrostatic pressure based on the density of water alone, *Pw*, and the measured thickness of the mixture above the sensor (equation (6)). Bold lines represent the theoretical value for pore pressure $P_w + P_s$ (equation (7)), again normalized by P_w and calculated using ρ_s for each mixture (Table 1). In other words, hydrostatic with respect to the density of the muddy fluid is represented by these lines. The uncertainty in these calculations reflected by the thickness of these lines is similar for all data sets (≈0.15), is associated primarily with the measured deposition height, and measurement uncertainty due to temperature effects is explained in section 2 (Methods). In three cases (marked with an asterisk in Figure 12) our "taring" process failed, so only relative pressure is known. Consequently, we shifted the measured values so that the pressure decays to predicted hydrostatic pressure ($P_w + P_s$) in 5 min, as discussed below.

In all cases the basal pressure, upon drum cessation, starts higher and decays to a lower value. The decay rate appears strongly dependent on grain size distribution. Importantly, the pressure dissipation for mixtures including a high fraction of fine particles was insignificant during the first 5 min. This indicates that the high degree of liquefaction observed during shearing is maintained over long timescales, and the fluid supports a substantial portion of the coarse particles even after the flow has stopped. The

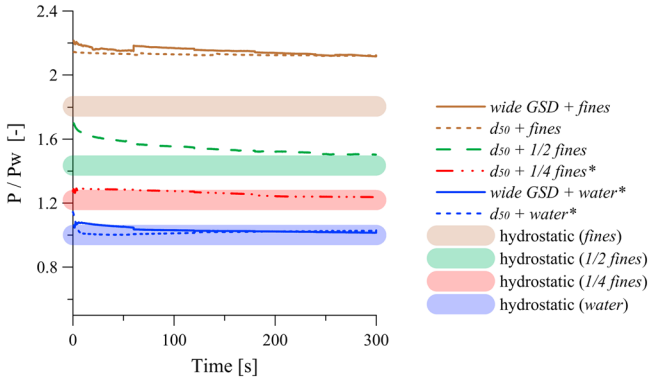

Figure 12. Basal fluid pressure dissipation in stationary mixtures, as determined after the flow had stopped. P is measured using the basal pressure sensors and normalized by calculated hydrostatic fluid pressure P_w (equation (6)). Bold lines represent the theoretical value for pore pressure $P_w + P_s$ (equation (7)), normalized by P_w and calculated using ρ_s for each mixture (Table 1) and roughly measured vertical deposition heights. The uncertainty in these calculations reflected by the thickness of these lines is similar for all data sets (≈0.15) is associated primarily with the measured deposition height and measurement uncertainty due to temperature effects explained in section 2 (Methods). Measurements marked with an asterisk in the legend have been visually adjusted as explained in the text.

decay rate increases with decreasing fine particle content. When fines are absent, fluid pressure after 5 min is close to a steady value, which we assume to be hydrostatic ($P_w + P_s$). While fine particles have the most significant role in maintenance of high pore pressure, our data for the two experiments performed without fine particles indicate that a wide grain size distribution in the coarse particles also delays pressure dissipation.

To estimate the diffusivity of excess pore pressures (D in equation (5)), as in *Major* [2000], we apply appropriate initial and boundary conditions to possible solutions to equation (5). The initial excess pressure is assumed to increase linearly with depth (from 0 at the top surface) and that there is a no-flux boundary condition at the base. The solution takes the form of

$$P_e(z,t) = 8P_{e,0}\sum_{n=0}^{\infty}\frac{1}{(2n+1)^2\pi^2}\cos(\lambda_n z)e^{-\lambda_n^2 Dt} \tag{12}$$

where $P_{e,0} = P_e(z=0, t=0)$, and it can be shown [e.g., *Fourier*, 1822] that $\lambda_n = [(\pi/L)(2n+1)/2]$. A fit of this equation to our basal pressure data (that is, $P - P_s - P_w$ versus $t=0$) gives an estimate for the hydraulic diffusivity of our mixtures D (Table 2). D varies from 10^{-2} m^2/s for d_{50} + water and decreases either with the addition of fines or with the widening of the GSD to 10^{-6} for the wide GSD + fines mixture.

4. Discussion

4.1. Scaling Issues

The large scale of our debris flows suggest that common scaling problems associated with particle size in laboratory experiments of debris flows (such as the relative importance of surface tension, cohesion, and viscous effects) are not significant. However, the largest particles we used (128 mm) are small compared to the largest particles in natural bouldery debris flows, and our flow depths are typically smaller than natural flows as well. To compare our investigations with other small and large-scale experiments, as well as with natural flows, we use a set of dimensionless parameters suggested by *Iverson et al.* [2010] and detailed by *Iverson* [2015]. Table 4 lists nine dimensionless parameters comprising geometric scaling ratios as well as different stress ratios and includes a modified Reynolds number, N_R (representing a measure of importance of fluid viscosity on bulk shear resistance), a fluid pressure number, N_P (comparing flow duration with the timescale of pressure dissipation) and a Savage number, N_S (assessing the importance of frictional versus collisional flow resistance). Definitions and magnitude estimates of these dimensionless ratios for different experiments and field-scale debris flows are shown in Table 4.

Compared with natural debris flows, in most small-scale experimental studies of debris flows (column 1 of Table 3) the normalized yield shear stress Y is much larger, representative Reynolds number N_R is much smaller, and the grain size to flow depth ratios ε' is much larger. Each of these differences is partly due to the fact that small-scale experimental flows are shallow (smaller H) compared to natural flows. Deeper flows of the same material would tend to be less influenced by fluid viscosity (i.e., larger N_R) and might be more affected by excess fluid pressure effects (i.e., N_P, the relative rate of pore pressure dissipation is smaller). Larger-scale experiments such as those in the USGS flume (column 2 of Table 3) and ours (column 3 of Table 3) have alleviated some of these scaling issues because the thickness is greater in these larger

Table 4. Comparison of Scaling Parameters for the Drum Experiments With Other Experimental Setups and Typical Full Scale Debris Flow

Scaling Parameter	Small-Scale Lab Flows[a]	USGS Flume[a]	Drum (This Study)[b]	Full Scale Flow $H = 3$ m[a]
$\varepsilon = H/L$	0.01	0.01	0.1	0.01
$R = \rho_b/\rho_0$	1	1	1	1
$R_f = \rho_s/\rho_0$	0.6	0.6	0.5–0.8	0.6
$C = \tau/(\rho_0 gH)$	0–0.5	0–0.5	0.04–0.3	0 – 0.5
$Y = \tau_y/(\rho_0 gH)$	10^{-1}	10^{-2}	8×10^{-4}	10^{-3}
$N_R = (\rho_0 H\sqrt{gL})/\eta$	3×10^3	1×10^5	10^3–10^4	3×10^6
$N_P = \sqrt{L/g}/(H^2/D)$	6×10^{-3}	2×10^{-4}	10^{-6}–10^{-2}	6×10^{-6}
$\varepsilon' = d/H$	0.3	0.03	0.03	0.003
$N_S = \rho_r . \gamma^2 d^2/(\sigma_{tot} - P)$	10^1	10^{-1}	10^{-3}–10^{-2}	10^{-3}

[a]Comparative values were taken from *Iverson et al*. [2010]. The definitions of parameters and variables are given in the Notation section.
[b]For our study we used estimates for the following: reference density $\rho_0 = \rho_b$; measured fluid yield stress $\tau_y = 5$ Pa; effective interstitial fluid viscosity η between 0.1 and 1 Pa s for the muddy mixtures. Additionally, we used the d_{50} (= 10 mm) as the characteristic grain diameter, measured $L \sim 2.5$ m, $H \sim 0.3$ m, $.\gamma = 5$–$15\ s^{-1}$, and $D = 10^{-2}$–$10^{-6}\ m^2/s$.

experiments. In large-scale experiments normalized yield stress may be less than an order of magnitude greater than in natural flows. N_R in our drum experiments is smaller than in other large-scale experiments and natural flows, indicating that the effect of fluid viscosity is more pronounced. This is important to consider when interpreting the strong effect of fluid viscosity on bulk flow resistance at high liquefaction ratios in our experiments (Figure 10). Due to the wide range of mixture compositions investigated, N_P varies in our study over 4 orders of magnitude, covering the range of natural debris flows. The average Savage number which indicates relative importance of collisional resistance to frictional contacts is similarly small as in natural debris flows, indicating a similar importance of frictional flow resistance [*Savage and Hutter*, 1989].

One significant difference between experiments in a straight flume and in a rotating drum is the aspect ratio, $\varepsilon = H/L$. An aspect ratio of $\varepsilon \ll 1$ is typically specified as the condition for the applicability of a shallow water assumption in depth-averaged model equations [*Savage and Hutter*, 1989]. *Mangeney-Castelnau et al*. [2005] tested the validity of the shallow water or thin layer approximation in depth-averaged model by comparing simulation and experiments of granular collapses with different aspect ratios. They show that reasonable agreement is found for aspect ratios lower or equal to 0.5–0.7. In the drum, flow depth values are typically about 0.25 to 0.3 m, but they are rather short flows with a flow length of around 2.1 to 2.8 m, resulting in a length ratio of $\varepsilon \sim 0.1$. This value may apply to debris flows in the initial stage, but is about 1 order of magnitude higher than that of fully developed flows and typical flume experiments [*Iverson et al*., 2010; *Kaitna et al*., 2014]. Therefore, stress gradients and bed-normal acceleration, especially at the front and the tail of the flow, are more pronounced (up to a factor of 10 more than in equivalent longer flows), which might have a significant effect on excess pressure generation. In this study we are neither attempting to reproduce entire debris flows nor are we attempting to establish a well-defined rheometric flow. Rather, our goal is to create physically realistic dynamics and kinematics of a portion of a flow, including the flow front and then compare the changes in system dynamics to certain changes in the grain size distribution to relate them to the effects of pore fluid pressure. The similarity of the dimensionless numbers from our experiments to those typical of natural flows indicate that we have set up a system where our data can serve to provide such a comparison that is relevant to natural debris flows.

4.2. Fluid Pressure and Bulk Flow Behavior

In our experiments, all mixtures with fine sediment, which included clay, silt, and sand, exhibited fluid pressures P in excess of those calculated from hydrostatic using the density of water alone P_w. When a hydrostatic pressure was calculated using a fluid density including the contribution of all fine particles up to 2 mm that might be in suspension ($P_w + P_s$), only the mixtures with abundant fines or a wide coarse particle GSD or both had measured fluid pressures above the theoretical hydrostatic value. Mixtures with both a narrow GSD and lower percentages of fine particles exhibited fluid pressures close to hydrostatic when accounting for fines in suspension ($P_w + P_s$) at the base of the flow. For these mixtures, fluid pressure measurements within the flow reveal that grain fluid segregation processes and bulk dilation due to shearing likely caused the region close

to the free surface to become unsaturated, leading to reduced basal fluid pressures. For two different flows with the same amount of fines (either a high fraction or none at all) but different coarse particle GSD's, the mixture with the wider GSD exhibited significantly higher average excess fluid pressures compared with the mixture with the narrow coarse particle GSD. We conclude that the development of excess fluid pressure in natural flows depends on the combination of the presence of fines [*Iverson et al*., 2010] as well as grain size distribution of the coarse sediment. These higher fluid pressures in poorly sorted material might also explain the observation of increased runout distances for small-scale laboratory flows having wider GSD as reported by *Bowman and Sanvitale* [2009] and *de Haas et al*. [2015].

Flows with high fine sediment content had increased fluid pressure relative to normal stress (i.e., high liquefaction ratios LR) and a reduced surface slope (Figure 10). This supports the importance of nonhydrostatic fluid pressures as a key parameter for debris flow mobility (*Iverson* [1997], and subsequent papers). However, the liquefaction ratio does not govern this behavior alone. In particular, the flow with the highest measured liquefaction ratio (LR = 0.85) was the uniform gravel mixture with the highest fraction of fine particles (d_{50} + fines) and a surface slope of 17.5°. Counterintuitively, both the surface angle and the LR were larger than those for the equivalent mixture having a wide GSD and a high fraction of fines (wide GSD + fines: surface slope = 7.7° and LR = 0.82). Removing fines from the wide GSD mixture reduced LR to that for hydrostatic water pressure and dramatically increased surface slope, while removing fines from the d_{50} mixture also reduced LR to that for hydrostatic water pressure, but slightly *increased* flow resistance. The presence of considerable fines corresponded to a high LR for both, the wide and narrow coarse particle size distribution, but had a substantially different effect on the mobility for the two systems. This observation is of special interest, as it reflects the interplay between flow resistances due to particle friction and due to resistance of the fluid, i.e., the suspension of water and particles. The variation in slopes for these high LR flows may be partly connected to a high sensitivity of the fluid flow resistance to minor variations in sediment concentration $C_{v,f}$, as commonly observed in rheologic studies on muddy suspensions [e.g., *Coussot*, 1997]. Probably over the duration of the experiment some small amount of water evaporated from the mixture resulting in a change in the interstitial fluid rheology. Such effects might become more evident at high values of LR, which in turn depends on the sediment concentration of the muddy fluid $C_{v,f}$. Similarly, *de Haas et al*. [2015] found in small-scale experiments that a low content of clay increased the runout of laboratory debris flows, and a high content of clay decreased the runout. We did not investigate the effect of changing the effective viscosity of the interstitial fluid on bulk flow resistance or LR, but note that earlier scaling considerations ($N_R \propto H$) imply that viscous effects on flow resistance might be less important in natural flows.

For mixtures having LR ~ 0.5 (d_{50} + water, d_{50} + ¼ fines) we found velocity profiles sheared over much of the flow depth (rather than having a narrow shear band) when fluid saturates the pores. In contrast, for the mixture with the highest fluid pressure (wide GSD + fines) and LR > 0.8, the shape of the velocity profile differed, with shear concentrated closer the bed and an unsheared region close to the surface. These observations are in accordance with measurements reported by *Kaitna et al*. [2014] and indicate a different source of flow resistance and constitutive flow behavior from one mixture to another. We hypothesize that for flows with lower LR, enduring grain contact stresses significantly affect flow behavior and a granular flow law, for which the bulk friction coefficient is a function of a dimensionless inertial number as suggested by *Boyer et al*. [2011] for granular suspensions, might apply. Importantly, in the absence of frictional resistance, i.e., LR → 1, other sources of flow resistance, like collisional interactions [*Iverson*, 2013] or viscous resistance of the fluid may govern flow behavior. The velocity profile measured for the wide GSD + fines does not show a typical granular scaling [*Kaitna et al*., 2014] and hence does not support a collisional flow model. It is likely that this experimental mixture fell in a regime where fluid properties (i.e., it is sensitive to changes in water content) strongly governed flow behavior and the complex non-Newtonian rheology of the suspension coarse sediment in the muddy fluid determined the velocity profile. The measured reduction in normalized basal normal stress fluctuations and fluid pressure fluctuations (Figure 9) support this argument. However, the unsheared region close to the surface of the wide GSD + fines mixture cannot be explained by the measured fluid yield stress alone, as the maximum height of a plug flow is estimated to be at the order of millimeter ($H_{\mathrm{plug}} = \tau_y/(\rho_b g \sin\theta) = 5/(2318 \times 9.81 \times \sin(7.8))$. We hypothesize that higher induced shear rates in this mixture, may lead to collisional interactions or turbulent effects [*Ancey*, 2006].

4.3. Excess Pressure Generation

Since all mixtures experienced the same flow conditions (characterized in terms of mean velocity, channel width, roughness, and curvature), we expect the same fluid pressure generation mechanisms to occur in mixtures exhibiting prolonged excess fluid pressures. We have shown that the effect of centrifugal acceleration is smaller than 5% of the total pressure and cannot explain the measured values of excess fluid pressure. *Hotta and Ohta* [2000] and *Hotta* [2011] argue that a dynamic component of fluid pressure arises due to Reynolds stresses associated with velocity fluctuations in water that is strongly sheared by particles. Application of their proposed model [*Hotta*, 2011, equation (9)] to our experiments with coarse sediment and water found that the predicted additional dynamic component would be on the order of only 10^1 Pascal, between 1 and 2 orders of magnitude smaller than the excess pressure measured. The presence of fine material is expected to dampen velocity fluctuations in the pore fluid, so we conclude that Reynolds stresses are not a significant generator of excess fluid pressure measured in our experiments.

The classic work of *Bagnold* [1954] showed that the pressure in sheared grain-fluid systems (not distinguishing between fluid and grain stresses) scales with the square of the shear rate, which Bagnold modeled as due to an increase in interparticle collisions. Free-surface experiments represent a different situation than that considered by *Bagnold* [1954], but there is still the question of whether collisional interactions of the solid phase have an effect on the generation of long-term excess fluid pressure. In our experiments we suspect this effect is minimal for two reasons. First, our average Savage numbers, N_S, are much smaller than 0.1 (Table 3), indicating relatively low stresses associated with interparticle collisions compared to those associated with frictional effects [*Savage and Hutter*, 1989]. Second, we find that prolonged excess fluid pressure is higher for the unsorted mixture (wide GSD + fines) for which there were also lower values of normalized stress and pressure fluctuations (Figure 9). In a natural debris flow, *McArdell et al*. [2007] measured both excess fluid pressures and impulses (independently recorded by geophones) associated with intermittent collisional stresses and also concluded that elevated fluid pressure was not being generated by strong particle agitation.

Iverson and George [2014] present a model framework that connects the dynamic evolution of pore fluid pressure with porosity changes due to changes in stress and dilatancy due to shearing. This is similar to a model framework presented by *Pailha and Pouliquen* [2009], but for brevity we focus on the details presented by *Iverson and George* [2014]. In this framework, changes in stress may lead to compaction or dilation of the particle network leading to pressure gradients in the pore fluid. For example, when the dense particle network is sheared, pore spaces have to increase, and fluid pressure decreases until sufficient fluid flows into the pores. When pore space decreases by contractive shearing, fluid pressure will rise until excess pressures diffuse. In their model, this process is represented by a dilation angle, i.e., volume change per shear strain, which is connected to a change in solid concentration. Iverson and George use this framework and an assumption that there is an equilibrium value of solid concentration for a given ambient stress state to calculate a dilation rate for given conditions. In this way, their model indicates that the instantaneous value of solid concentration with respect to solid concentration at equilibrium for a given stress state and flow rate is of major importance for the evolution of fluid pressure at the onset of shearing.

A physical interpretation of this model framework leads us to the hypothesis that there should be at least three mechanisms that lead to porosity changes and excess fluid pressure generation in debris flows:

1. Positive or negative dilation of debris due to shearing at the onset of motion. This situation is of special importance for debris flows initiating from landslides and probably less important for debris flows developing progressively from channel erosion. In our experiments we did not investigate the dynamics during initiation, but we suspect the influence of initial conditions on excess pore pressure were minimal;
2. Deformation of the bulk due to the typically unsteady nature of the flow might dilate or contract pore spaces when debris transits natural channels over long distances. For our steady experimental flows in the drum, bulk contraction and elongation in connection to changes of overall surge geometry are expected to be less important;
3. In nonuniform flows some volume elements of debris might undergo contraction and elongation as material at the surface travels at higher speeds than the mean velocity and is overridden (and contracted) at the front and probably later incorporated into the flow again. In the rotating drum these transient contraction and dilation cycles are eminent and more pronounced as flows are short (aspect ratio $\varepsilon \sim 0.1$) compared with natural flows and flume experiments (aspect ratio $\varepsilon \sim 0.01$). The presence of an

unsaturated front [*Kaitna et al*., 2011; *Leonardi et al*., 2015] might obscure these circulation patterns, but the saturated material behind the front is necessarily subject to vertical accelerations that might affect fluid pressures throughout the flow.

In all cases, pore pressure may remain elevated when hydraulic diffusivity of the mixture is low. Guided by dimensional analysis as outlined by *Iverson and LaHusen* [1989], *Goren et al*. [2010], *McCoy et al*. [2012], and *Iverson and George* [2014], we estimate timescales of these three pressure generation mechanisms and the timescales for pressure diffusion to identify their relative importance in the laboratory and in the field. The timescale for porosity change at the particle scale due to shearing is

$$T_{\text{shear}} = 1/\dot{\gamma} \tag{13}$$

In our flows we measured steady shear rates mostly between $\dot{\gamma} \sim 5$–$15\ \text{s}^{-1}$, so the relevant T_{shear} in our experiments ranges from 10^{-2} to 10^{-1} s. Shear rates of natural flows are probably in a similar range [*Iverson and Denlinger*, 2001]. Since dilative shearing is especially important at the onset of shearing, we conclude that 10^{-2} s is a lower bound for T_{shear} in natural flows.

The timescale of repeated frontal contraction based on the recirculation pattern in the drum (i.e., the time of a particular sediment traveling from the snout to the tail and then back to the snout) we calculate with

$$T_{\text{fc,drum}} = 2L/V_m\ , \tag{14a}$$

which yields $T_{\text{fc,drum}} \sim 4$ s. For natural debris flows regular recirculation patterns as in the drum are unlikely; however, to estimate a timescale for the effect of contraction by overriding action at the front, we argue that a volume element of material involved in a debris flow is transported and overridden at the front at least once during an event. Hence,

$$T_{\text{fc,DF}} = L/V_m\ . \tag{14b}$$

We infer length and mean velocity of debris flow surges in alpine regions from hydrographs reported by *Arai et al*. [2013] with 100–500 m and 5–10 m/s, respectively, and calculate an upper bound of $T_{\text{fc,DF}} \sim 10^1$ s, which is 1 order of magnitude longer than in our experiments.

The average timescale due to unsteady motion induced by bulk elongation/contraction or channel geometry is expected to be highly variable; here we estimated that T_{geo} is on the order of 10^0 to 10^1 s for natural flows and not relevant in our drum experiments.

We compute the average duration of pressure dissipation over the flow thickness H according to

$$T_{\text{diss}} = \mathscr{L}^2/D\ , \tag{15}$$

where $\mathscr{L}$ is the length scale for pressure diffusion. In section 3 we calculated diffusion coefficients from basal pressure diffusion after cessation of movement using the length scale of the deposition height. For constantly deforming mixtures, the choice of an appropriate length scale is not obvious as pore spaces might constantly increase and decrease. Conservatively for a flowing mixture $\mathscr{L}$ might be between the length scale of a grain (e.g., the d_{50}) and the flow depth H. Hence, for calculating T_{diss} in our experiments, we considered $\mathscr{L}$ to vary between 0.01 m and 0.25 m. For the mixture d_{50} + water ($D = 10^{-2}\ \text{m}^2/\text{s}$) we estimate a dissipation timescale $T_{\text{diss, d50}}$ between 10^{-2} and 6 s, which is in the range of timescales of pressure generation mechanism described earlier. For the other extreme—the mixture GSD + fines ($D = 10^{-6}\ \text{m}^2/\text{s}$)—we estimate timescales $T_{\text{diss, wGSD}}$ between 10^2 and 10^4 s (minutes to hours), which is orders of magnitude longer than pressure generation mechanism. Note that diffusion timescales for deeper flows, $T_{\text{diss, DF}}$, may be significantly larger [*Iverson*, 2015].

Though the appropriate length scale for pressure dissipation in constantly deforming grain-fluid mixtures is difficult to assess, we see that the timescales of pressure generation are typically shorter than the timescale of pressure dissipation. Only in very porous, shallow flows, pressure dissipation might be on a similar timescale as the timescale of shearing, like our uniform gravel mixture with limited fines, and probably the experiments presented by *Iverson and LaHusen* [1989]. Importantly, pressure generation mechanism discussed herein are independent of mixture composition, and therefore, we conclude that the primary manner in which GSD controls excess pore pressure is in (limiting) pore pressure dissipation rather than in generating excess pore pressure.

4.4. Excess Pressure Dissipation and Hindered Settling

We hypothesize that the excess pore pressure we measured after the flow stopped moving was the result of the cumulative effect of grains settling against a viscous fluid and the effect is likely similar in the deposition of material from a field-scale debris flow. When particles settle at a steady velocity (essentially, a terminal velocity) in a fluid, their weights are balanced by fluid forces until coming to rest on a boundary or another grain-grain chain that is ultimately resting on a boundary. On the bulk scale, consolidation theory may be a useful tool to describe the diffusion of excess fluid pressure [*Major*, 2000]. On the particle scale, three mechanisms may operate. Fine particles that are suspended in the pore fluid are expected to alter effective fluid properties like density and viscosity [*Coussot*, 1997]. Second, at higher particle concentrations the presence of adjacent grains induces larger drag and reduces settling velocities compared to isolated particles settling in clear water. This effect is often termed *hindered settling* and can be estimated by various empirical equations suggested in the literature [e.g., *Garcia*, 2008]. Applying a relation proposed by *Soulsby* [1997] for hindered settling velocity to the fine fraction of our muddy flows, using a mean $d_{\text{fines}} = 0.02$ mm and $C_{v,f} = 0.4$, we find that the settling velocity of fine sediment is reduced by more than an order of magnitude compared to the settling velocity of a single particle of the same size. A third mechanism to keep particles in suspension is due to a finite yield stress of fluids which contain a sufficiently high fraction of clay particles [*Hampton*, 1979; *Beris et al*., 1985; *Tabuteau et al*., 2007]. Assuming the grains are spherical with a radius r_o, the weight of the submerged particle, F_{SP}, for a given grain size is

$$F_{SP} = \frac{4}{3}\pi(\rho_r - \rho_s)g{r_o}^3 \tag{16}$$

For our mixtures with fine sediment, ρ_s is around 1800 kg/m^3 and the density of the sediment ρ_r is assumed to be 2650 kg/m^3. In such a mixture a sphere of radius r_o will sink when the yield stress parameter, Y_g,

$$Y_g = \frac{2\tau_y\pi{r_o}^2}{F_{SP}} \tag{17}$$

is less than 0.143 [*Beris et al*., 1985]. Using measured yield stress of 5 Pa and solving for the critical radius at which grains will move, r_c,

$$r_c = \frac{2\tau_y}{0.143\left({}^4/_3\right)(\rho_r - \rho_s)g} \tag{18}$$

we find that grains ~6 mm in diameter or less will be supported by the fluid (which is close to the median grain size of 10 mm of both mixtures), and those greater will sink. With regards to debris flow modeling, the question of a threshold grain diameter separating sediment belonging to the solid or the fluid is therefore strongly connected to mixture composition.

5. Conclusions

Large-scale rotating drum experiments reveal that for debris flow mixtures the grain size distribution (GSD) of the coarse fraction as well as the presence of fines in the fluid strongly influence the presence of sustained excess fluid pressure. In particular, fluid pressures in excess of hydrostatic developed in all mixtures where fines were present. When accounting for fine sediment in suspension, the proportion of excess fluid pressure on measured fluid pressure reduces. Using a cutoff diameter of 2 mm, only the mixtures with largest fines content exhibited excess fluid pressure. When coarse sediment was composed of a poorly sorted mixture, excess fluid pressure extended through the entire flow length. For these mixtures, pore pressures and theoretical considerations indicate that particles up to small gravel were fully supported by the fluid.

Bulk flow resistance, as expressed by the steady state surface profile of the flows, tended to decrease with increasing liquefaction ratio LR, defined as the ratio of fluid pressure to basal total normal stress. Dry flow had a slope of 33° and saturated with water slopes dropped to about 23° (for LR of 0.44). The progressive increase in fines in the fluid reduced the slope to ~18° (for LR of ~0.6 to 0.85). The combination of a wide GSD and elevated fines in the fluid dropped the surface slope to as low as ~8° (for LR of 0.82). At the highest LR wide slope variation from 8 to 18° may reflect the dominance of fluid flow resistance and resulting high sensitivity to small changes in water content

Measurements of vertical distribution of velocity and pore fluid pressure show that with increasing fines content, shear concentrates in the lower layers of the flow where the fluid pressure was highest. This observation supports the notion of a transition from a frictional flow regime when LR is low and to a flow behavior for unsorted debris including fine sediment when LR approaches 1 for which flow resistance is decoupled from effective normal stress.

We find that generation of excess fluid pressure in our experiments does not substantially arise from centripetal acceleration or Reynolds stresses. There is also no indication that collisional interactions generate sustained excess pore pressure, as normalized stress and pressure fluctuations decrease with increasing excess fluid pressure. Rather, we associate the generation of high fluid pressure in our experiments with the contraction of pore spaces due to the nonuniform flow pattern at the front of the flows, where material is overridden and dragged back into the flow—a process that is also evident and probably also important in nature. Other mechanisms that may lead to porosity changes and nonhydrostatic fluid pressure, like contractive/dilative shearing at the onset of motion or bulk elongation/contraction during flow, might be important in natural flows but are less relevant in our experiments. Since timescales of pressure generation are relatively constant, independent of material composition and mostly short, we conclude that the primary manner in which GSD (including the presence of fines in the fluid) controls excess pore pressure is in limiting pore pressure dissipation. This limit may arise from reduced settling of coarser particles through a dense fluid that hinders settling and may have a yield strength.

Notation

C	dimensionless basal shear stress (-).
$C_{v,b}$	volumetric sediment concentration relative to the entire mixture (-).
$C_{v,c}$	volumetric sediment concentration of coarse particles relative to the entire mixture (-).
$C_{v,f}$	volumetric sediment concentration of fine particles relative to the entire mixture (-).
d	grain diameter (m).
d_{50}	50th percentile diameter of the coarse fraction (m).
D	hydraulic diffusivity (m^2/s).
E_c	bulk stiffness modulus (Pa).
F_B	buoyancy force (N).
F_{SP}	weight of a submerged particle (N).
g	acceleration due to gravity (m/s^2).
H	flow depth (m).
k	hydraulic permeability of the porous media (m^2).
L	flow length (m).
$\mathscr{L}$	length scale for pressure dissipation (m).
LR	liquefaction ratio (-)
N_R	modified Reynolds number (-).
N_P	fluid pressure number (-).
N_S	Savage number (-).
P	measured fluid pressure (Pa).
P_w	hydrostatic fluid pressure (Pa).
P_s	fluid pressure component due to fines in suspension (Pa).
P_{ca}	fluid pressure component due centrifugal acceleration (Pa).
P_e	excess pore fluid pressure (Pa).
$\tilde{P}_e$	excess pressure ratio (-).
R	density ratio (-).
R_f	fluid density ratio (-).
r_0, r_c	sphere radius, critical sphere radius (m).
T_{shear}	timescale of particle rearrangement (s).
T_{fc}	timescale of material recirculation (s).
T_{geo}	timescale of unsteady motion (s).
T_{diss}	timescale of excess pore pressure dissipation (s).

V_m mean drum velocity at the circumference (m/s).
Y dimensionless yield stress (-).
Y_g yield stress parameter (-).
z bed normal coordinate (m).
θ local surface slope (deg).
ε aspect ratio (-).
ε' relative grain size (-).
$\dot{\gamma}$ shear rate (s^{-1}).
η dynamic viscosity of the pore fluid (Pa s).
ρ_b bulk density (kg/m^3).
ρ_0 reference density (kg/m^3).
ρ_s fluid density (kg/m^3).
ρ_r solid (rock) density (kg/m^3).
ρ_w water density (kg/m^3).
σ_{eff} effective normal stress (Pa).
σ_{tot} total normal stress (Pa).
τ basal shear stress (Pa).
τ_y yield stress (Pa).

Acknowledgments
The authors would like to thank Michael Manga, Leslie Hsu, Leonard Sklar, Fritz Zott, Chris Ellis, Jim Mullin, and Stuart Foster for insightful discussions and help with sensor development and drum experiments. We particularly thank Anne Mangeney for insightful and critical review that significantly improved the manuscript. We also thank Michael Manga and Max Rudolph for training and use of the Haake Rheoscope1 for our rheology measurements. The discussion of the contraction and dilation cycles was inspired by an anonymous reviewer comment. This work was supported by the STC program of the National Science Foundation via the National Center for Earth-Surface Dynamics under the agreement EAR-0120914 the National Science Foundation grant CBET-0932735, and the Austrian Science Fund (J2837-N10). Marisa Palucis was partially supported by the Jet Propulsion Laboratory, California Institute of Technology, under a contract with NASA under the Mars Program Office. The experimental data may be obtained from R.K. (roland.kaitna@boku.ac.at).

References

Ahn, H., C. E. Brennen, and R. H. Sabersky (1991), Measurements of velocity, velocity fluctuation, density, and stresses in chute flows of granular materials, *Trans. ASME E: J. Appl. Mech.*, *58*, 792–803.
Ancey, C. (2006), Plasticity and geophysical flows: A review, *J. Non-Newton. Fluid.*, *142*, 4–35, doi:10.1016/j.jnnfm.2006.05.005.
Ancey, C., and P. Evesque (2000), Frictional-collisional regime for granular suspension flows down an inclined channel, *Phys. Rev.*, *62*(6), 8349–8360.
Arai, M., J. Huebl, and R. Kaitna (2013), Occurrence conditions of roll waves for three grain–fluid models and comparison with results from experiments and field observation, *Geophys. J. Int.*, doi:10.1093/gji/ggt352.
Armanini, A., H. Capart, L. Fraccorollo, and M. Larcher (2005), Rheological stratification in experimental free-surface flows of granular-liquid mixtures, *J. Fluid Mech.*, *532*, 269–319, doi:10.1017/S0022112005004283.
Bagnold, R. A. (1954), Experiments on a gravity-free dispersion of large solid spheres in a Newtonian fluid under shear, *Proc. R. Soc. London, Ser. A*, *225*, 49–63.
Berger, C., B. W. McArdell, B. Fritschi, and F. Schlunegger (2010), A novel method for measuring the timing of bed erosion during debris flows and floods, *J. Geophys. Res.*, *116*, F01002, doi:10.1029/2010JF001722.
Beris, A. N., J. A. Tsamopoulos, R. C. Armstrong, and R. A. Brown (1985), Creeping motion of a sphere through a Bingham plastic, *J. Fluid Mech.*, *158*, 219–244.
Berti, M., and A. Simoni (2005), Experimental evidences and numerical modeling of debris flow initiated by channel runoff, *Landslides*, *2*, 171–182, doi:10.1007/s10346-005-0062-4.
Berti, M., R. Genevois, A. Simoni, and P. R. Tecca (1999), Field observations of a debris flow event in the Dolomites, *Geomorphology*, *29*, 265–274, doi:10.1016/S0169-555X(99)00018-5.
Berzi, D., and J. T. Jenkins (2009), Steady inclined flows of granular-fluid mixtures, *J. Fluid Mech.*, *641*, 359–387, doi:10.1017/S0022112009991510.
Bouchut, F., E. D. Fernandez-Nieto, A. Mangeney, and G. Narbona-Reina (2015), A two-phase shallow debris flow model with energy balance, *Math. Modell. Numer. Anal.*, *49*, 101–140, doi:10.1051/m2an/2014026.
Bowman, E. T., and N. Sanvitale (2009), The role of particle size in the flow behavior of saturated granular materials, in *Proceedings of the 17th International Conference on Soil Mechanics and Geotechnical Engineering*, edited by M. Hamza, M. Shahien, and Y. El-Mossallamy, pp. 170–173, IOS Press, Amsterdam, Netherlands, doi:10.3233/978-1-60750-031-5-470.
Boyer, F., E. Guazzelli, and O. Pouliquen (2011), Unifying suspension and granular rheology, *Phys. Rev. Lett.*, *107*, 188301, doi:10.1103/PhysRevLett.107.188301.
Chen, H., D. Su, and K. Chen (2001), Some case studies on the engineering geological characteristics of debris flows in Taiwan, *West. Pac. Earth Sci.*, *1*(3), 265–296.
Chow, V. T. (1959), *Open-Channel Hydraulics*, *Civil Engineering Ser.*, McGraw Hill, New York.
Costa, J. E. (1984), Physical geomorphology of debris flows, in *Developments and Applications of Geomorphology*, edited by J. E. Costa and P. J. Fleischer, pp. 268–317, Springer, Berlin.
Coussot, P. (1997), *Mudflow Rheology and Dynamics*, *IAHR Monogr. Ser.*, Balkema, Rotterdam.
Coussot, P., and C. Ancey (1999), Rheophysical classification of concentrated suspensions and granular pastes, *Phys. Rev. E*, *59*, 4445–4457.
Darcy, H. (1856), *Les Fontaines Publiques de la Ville de Dijon*, Dalmont, Paris.
de Haas, T., L. Braat, J. R. Leuven, I. R. Lokhorst, and M. G. Kleinhans (2015), Effects of debris flow composition on runout, depositional mechanisms, and deposit morphology in laboratory experiments, *J. Geophys. Res. Earth Surf.*, *120*, 1949–1972, doi:10.1002/2015JF003525.
Fan, Y., and K. M. Hill (2011), Theory for shear-induced segregation of dense granular mixtures, *New J. Phys.*, *13*, 095009.
Farin, M., A. Mangeney, and O. Roch (2014), Fundamental changes of granular flow dynamics, deposition and erosion processes at high slope angles: Insights from laboratory experiments, *J. Geophys. Res. Earth Surf.*, *119*, 504–532, doi:10.1002/2013JF002750.
Fourier, J. (1822), *Théorie analytique de la chaleur*, Firmin Didot Père et Fils, Paris.

Garcia, M. H. (2008), Sediment transport and morphodynamics, in *Sedimentation Engineering: Processes, Measurements, Modeling, and Practice*, *ASCE Manuals and Reports on Engineering Practice*, vol. 110, edited by M. H. Garcia, Am. Soc. of Civ. Engineers, Reston, Va., doi:10.1061/40856(200)94.

Groupement de Recherche Milieux Divisés (2004), On dense granular flows, *Eur. Phys. J. E*, *14*, 314–365, doi:10.1140/epje/i2003-10153-0.

Goren, L., E. Aharonov, D. Sparks, and R. Toussaint (2010), Pore pressure evolution in deforming granular material: A general formulation and the infinitely stiff approximation, *J. Geophys. Res.*, *115*, B09216, doi:10.1029/2009JB007191.

Hampton, M. A. (1979), Buayancy in debris flows, *J. Sediment. Petrol.*, *49/3*, 753–758.

Herschel, W. H., and R. Bulkley (1926), Konsistenzmessungen von Gummi-Benzollösungen, *Kolloid Z.*, *39*, 291–300, doi:10.1007/BF01432034.

Hill, K. M., and D. Tan (2014), Theory for segregation in dense sheared flows: Gravity, temperature gradients, and stress partitioning, *J. Fluid Mech.*, *756*, 54–88.

Hill, K. M., and B. Yohannes (2011), Rheology of dense granular mixtures: Boundary pressures, *Phys. Rev. Lett.*, *106*, 058302, doi:10.1103/PhysRevLett.106.058302.

Hotta, N. (2011), Pore water pressure distributions of granular mixture flow in a rotating mill, in *Italian Journal of Engineering Geology and Environment*, edited by R. Genevois, D. L. Hamilton, and A. Prestininzi, pp. 319–330, Sapienza Universita Editrice Univ. Press, Rome, Italy, doi:10.4408/IJEGE.2011-03.B-037.

Hotta, N., and T. Ohta (2000), Pore-water pressure of debris flows, *Phys. Chem. Earth. Partt. B.*, *25*(4), 381–386.

Hsu, L. (2010), Bedrock erosion by granular flow, PhD Dissertation, Department of Earth and Planet. Sci., Univ. of Calif., Berkeley.

Hsu, L., W. E. Dietrich, and L. S. Sklar (2008), Experimental study of bedrock erosion by granular flows, *J. Geophys. Res.*, *113*, F02001, doi:10.1029/2007JF000778.

Hsu, L., W. E. Dietrich, and L. S. Sklar (2014), Mean and fluctuating basal forces generated by granular flows: Laboratory observations in a large vertically rotating drum, *J. Geophys. Res. Earth Surf.*, *119/6*, 1283–1309, doi:10.1002/2013JF003078.

Hungr, O. (1995), A model for the runout analysis of rapid flow slides, debris flows, and avalanches, *Can. Geotech. J.*, *32*, 610–623, doi:10.1139/t95-063.

Hungr, O., S. G. Evans, M. J. Bovis, and J. N. Hutchinson (2001), A review of the classification of landslides of the flow type, *Environ. Eng. Geosci.*, *7*(3), 221–238.

Iverson, R. M. (1997), The physics of debris flows, *Rev. Geophys.*, *35*(3), 245–296, doi:10.1029/97RG00426.

Iverson, R. M. (2005), Regulation of landslide motion by dilatancy and pore pressure feedback, *J. Geophys. Res.*, *110*, F02015, doi:10.1029/2004JF000268.

Iverson, R. M. (2013), Mechanics of debris flows and rock avalanches, in *Handbook of Environmental Fluid Dynamics*, vol. 1, edited by H. J. S. Fernando, pp. 573–587, CRC Press Taylor Francis, Boca Raton.

Iverson, R. M. (2015), Scaling and design of landslide and debris-flow experiments, *Geomorphology*, *244*, 9–20, doi:10.1016/j.geomorph.2015.02.033.

Iverson, R. M., and R. P. Denlinger (2001), Flow of variably fluidized granular masses across three-dimensional terrain: 1. Coulomb mixture theory, *J. Geophys. Res.*, *106*(B1), 537–552.

Iverson, R. M., and D. L. George (2014), A depth-averaged debris-flow model that includes the effects of evolving dilatancy. I. Physical basis, *Proc. R. Soc. London, Ser. A*, *470*(2170), doi:10.1098/rspa.2013.0819.

Iverson, R. M., and R. G. LaHusen (1989), Dynamic pore-pressure fluctuations in rapidly shearing granular materials, *Science*, *246*(4931), 796–799, doi:10.1126/science.246.4931.796.

Iverson, R. M., M. Logan, R. G. LaHusen, and M. Berti (2010), The perfect debris flow? Aggregated results from 28 large-scale experiments, *J. Geophys. Res.*, *115*, F03005, doi:10.1029/2009JF001514.

Iverson, R. M., M. E. Reid, M. Logan, R. G. LaHusen, J. W. Godt, and J. P. Griswold (2011), Positive feedback and momentum growth during debris-flow entrainment of wet bed sediment, *Nat. Geosci.*, *4*, 116–121, doi:10.1038/ngeo1040.

Johnson, A., and J. Rodine (1984), Debris flow, in *Slope Instability*, edited by D. Brunsden and D. B. Prior, pp. 257–361, Wiley, Chichester.

Johnson, A. M. (1970), *Physical Processes in Geology: A Method for Interpretation of Natural Phenomena; Intrusions in Igneous Rocks, Fractures, and Folds, Flow of Debris and Ice*, Freeman Cooper, San Francisco, Calif.

Johnson, C. G., B. P. Kokelaar, R. M. Iverson, M. Logan, R. G. LaHusen, and J. M. N. T. Gray (2012), Grain-size segregation and levee formation in geophysical mass flows, *J. Geophys. Res.*, *117*, F01032, doi:10.1029/2011JF002185.

Jop, P., Y. Forterre, and O. Pouliquen (2006), A constitutive law for dense granular flows, *Nature*, *441*, 727–730, doi:10.1038/nature04801.

Kaitna, R., L. Hsu, D. Rickenmann, and W. E. Dietrich (2011), On the development of an unsaturated front of debris flows, in *Italian Journal of Engineering Geology and Environment*, edited by R. Genevois, D. L. Hamilton, and A. Prestininzi, pp. 351–358, doi:10.4408/IJEGE.2011-03.B-040.

Kaitna, R., W. E. Dietrich, and L. Hsu (2014), Surface slopes, velocity profiles and fluid pressure in coarse-grained debris flows saturated with water and mud, *J. Fluid Mech.*, *741*, 277–403, doi:10.1017/jfm.2013.675.

Kern, M. A., F. Tiefenbacher, and J. N. McElwaine (2004), The rheology of snow in large chute flows, *Cold Reg. Sci. Technol.*, *39*, 181–192, doi:10.1016/j.coldregions.2004.03.006.

Kowalski, J., and J. N. McElwaine (2013), Shallow two-component gravity-driven flows with vertical variation, *J. Fluid Mech.*, *714*, 434–462, doi:10.1017/jfm.2012.489.

Leonardi, A., M. Cabrera, F. K. Wittel, R. Kaitna, M. Mendoza, W. Wu, and H. J. Herrmann (2015), Granular front formation in free-surface flow of concentrated suspensions, *Phys. Rev. E*, *92*, 052204, doi:10.1103/PhysRevE.92.052204.

Louge, M., M. Tuccio, E. Lander, and P. Connors (1996), Capacitance measurements of the volume fraction and velocity of dielectric solids near a grounded wall, *Rev. Sci. Instrum.*, *67*, 1869, doi:10.1063/1.1146991.

Major, J. J. (2000), Gravity-driven consolidation of granular slurries—Implications for debris-flow deposition and deposit characteristics, *J. Sediment. Res.*, *70*(1), 64–83.

Major, J. J., and R. M. Iverson (1999), Debris-flow deposition: Effects of pore-fluid pressure and friction concentrated at flow margins, *Geol. Soc. Am. Bull.*, *111*(10), 1424–1434.

Mangeney, A., O. Roche, O. Hungr, N. Mangold, G. Faccanoni, and A. Lucas (2010), Erosion and mobility in granular collapse over sloping beds, *J. Geophys. Res.*, *115*, F03040, doi:10.1029/2009JF001462.

Mangeney-Castelnau, A., B. Bouchut, J. P. Vilotte, E. Lajeunesse, A. Aubertin, and M. Pirulli (2005), On the use of Saint-Venant equations for simulating the spreading of a granular mass, *J. Geophys. Res.*, *110*, B09103, doi:10.1029/2004JB003161.

McArdell, B. W., P. Bartelt, and J. Kowalski (2007), Field observations of basal forces and fluid pressure in a debris flow, *Geophys. Res. Lett.*, *34*, L07406, doi:10.1029/2006GL029183.

McCoy, S. W., J. W. Kean, J. A. Coe, D. M. Staley, T. A. Wasklewicz, and G. E. Tucker (2010), Evolution of a natural debris flow: In situ measurements of flow dynamics, video imagery, and terrestrial laser scanning, *Geology*, *38*, 735–738, doi:10.1130/G30928.1.

McCoy, S. W., J. W. Kean, J. A. Coe, G. E. Tucker, D. M. Staley, and T. A. Wasklewicz (2012), Sediment entrainment by debris flows: In situ measurements from the headwaters of a steep catchment, *J. Geophys. Res.*, *117*, F03016, doi:10.1029/2011JF002278.

Mueller, S., E. Llewellin, and H. Mader (2009), The rheology of suspensions of solid particles, *Proc. R. Soc. London, Ser. A*, doi:10.1098/rspa.2009.0445.
O'Brien, J., P. Julien, and W. Fullerton (1993), Two-dimensional water flood and mudflow simulation, *J. Hydraul. Eng.*, *119*, 244–261.
Pailha, M., and O. Pouliquen (2009), A two-phase flow description of the initiation of underwater granular avalanches, *J. Fluid Mech.*, *633*, 115–135.
Palucis, M. C. (2014), Using quantitative topographic analysis to understand the role of water on transport and deposition processes on crater walls, PhD Dissertation, Department of Earth and Planet. Sci., Univ. of Calif., Berkeley.
Pelanti, M., F. Bouchut, and A. Mangeney (2008), A Roe-type scheme for two-phase shallow granular flows over variable topography, *Math. Modell. Numer. Anal.*, *42*, 851–885, doi:10.1051/m2an:2008029.
Pierson, T. C. (1981), Dominant particle support mechanisms in debris flows at Mt Thomas, New Zealand, and implications for flow mobility, *Sedimentology*, *28*, 49–60.
Pierson, T. C. (1986), Flow behavior of channelized debris flows, Mount St. Helens, Washington, in *Hillslope Processes*, edited by A. D. Abrahams, pp. 269–296, Allen and Unwin, Boston.
Pitman, E. B., and L. Le (2005), A two-fluid model for avalanche and debris flows, *Philos. Trans. R. Soc., A*, *363*, 1573–1601.
Rickenmann, D. (1999), Empirical relationships for debris flows, *Nat. Hazards*, *19*, 47–77.
Rognon, P. G., J.-N. Roux, M. Naaïm, and F. Chevoir (2007), Dense flows of bidisperse assemblies of disks down an inclined plane, *Phys. Fluids*, *19*, 058101, doi:10.1063/1.2722242.
Savage, S. B., and K. Hutter (1989), The motion of a finite mass of granular material down a rough incline, *J. Fluid Mech.*, *199*, 177–215.
Schneider, D., R. Kaitna, L. Hsu, B. W. McArdell, and C. Huggel (2011), Rock-ice avalanches: Frictional behavior of granular rock-ice mixtures in vertically rotating drum experiments, *Cold Reg. Sci. Technol.*, doi:10.1016/j.coldregions.2011.07.001.
Soulsby, R. L. (1997), *Dynamics of Marine Sands*, Thomas Telford, London, U. K.
Tabuteau, H., P. Coussot, and J. R. de Bruyn (2007), Drag force on a sphere in steady motion through a yield stress fluid, *J. Rheol.*, *51*, 125–137, doi:10.1122/1.2401614.
Takahashi, T. (1991), *Debris Flow*, *IAHR Monogr. Ser.*, Balkema, Rotterdam.
Terzaghi, K. (1943), *Theoretical Soil Mechanics*, John Wiley, New York.
Tripathi, A., and D. V. Khakhar (2011), Rheology of binary granular mixtures in the dense flow regime, *Phys. Fluids*, *23*, 113302.
Yohannes, B., and K. M. Hill (2010), Rheology of dense granular mixtures: Particle-size distributions, boundary conditions, and collisional time scales, *Phys. Rev. E*, *82*, 061301, doi:10.1103/PhysRevE.82.061301.
Yohannes, B., L. Hsu, W. E. Dietrich, and K. M. Hill (2012), Boundary stresses due to impacts from dry granular flows, *J. Geophys. Res.*, *117*, F02027, doi:10.1029/2011JF002150.